

Observation of the rare $B_s^0 \rightarrow \mu^+ \mu^-$ decay from the combined analysis of CMS and LHCb data

The CMS and LHCb collaborations*

The standard model of particle physics describes the fundamental particles and their interactions via the strong, electromagnetic and weak forces. It provides precise predictions for measurable quantities that can be tested experimentally. The probabilities, or branching fractions, of the strange B meson (B_s^0) and the B^0 meson decaying into two oppositely charged muons (μ^+ and μ^-) are especially interesting because of their sensitivity to theories that extend the standard model. The standard model predicts that the $B_s^0 \rightarrow \mu^+ \mu^-$ and $B^0 \rightarrow \mu^+ \mu^-$ decays are very rare, with about four of the former occurring for every billion B_s^0 mesons produced, and one of the latter occurring for every ten billion B^0 mesons¹. A difference in the observed branching fractions with respect to the predictions of the standard model would provide a direction in which the standard model should be extended. Before the Large Hadron Collider (LHC) at CERN² started operating, no evidence for either decay mode had been found. Upper limits on the branching fractions were an order of magnitude above the standard model predictions. The CMS (Compact Muon Solenoid) and LHCb (Large Hadron Collider beauty) collaborations have performed a joint analysis of the data from proton–proton collisions that they collected in 2011 at a centre-of-mass energy of seven teraelectronvolts and in 2012 at eight teraelectronvolts. Here we report the first observation of the $B_s^0 \rightarrow \mu^+ \mu^-$ decay, with a statistical significance exceeding six standard deviations, and the best measurement so far of its branching fraction. Furthermore, we obtained evidence for the $B^0 \rightarrow \mu^+ \mu^-$ decay with a statistical significance of three standard deviations. Both measurements are statistically compatible with standard model predictions and allow stringent constraints to be placed on theories beyond the standard model. The LHC experiments will resume taking data in 2015, recording proton–proton collisions at a centre-of-mass energy of 13 teraelectronvolts, which will approximately double the production rates of B_s^0 and B^0 mesons and lead to further improvements in the precision of these crucial tests of the standard model.

Experimental particle physicists have been testing the predictions of the standard model of particle physics (SM) with increasing precision since the 1970s. Theoretical developments have kept pace by improving the accuracy of the SM predictions as the experimental results gained in precision. In the course of the past few decades, the SM has passed critical tests derived from experiment, but it does not address some profound questions about the nature of the Universe. For example, the existence of dark matter, which has been confirmed by cosmological data³, is not accommodated by the SM. It also fails to explain the origin of the asymmetry between matter and antimatter, which after the Big Bang led to the survival of the tiny amount of matter currently present in the Universe^{3,4}. Many theories have been proposed to modify the SM to provide solutions to these open questions.

The B_s^0 and B^0 mesons are unstable particles that decay via the weak interaction. The measurement of the branching fractions of the very rare decays of these mesons into a dimuon ($\mu^+ \mu^-$) final state is especially interesting.

At the elementary level, the weak force is composed of a ‘charged current’ and a ‘neutral current’ mediated by the W^\pm and Z^0 bosons,

respectively. An example of the charged current is the decay of the π^+ meson, which consists of an up (u) quark of electrical charge $+2/3$ of the charge of the proton and a down (d) antiquark of charge $+1/3$. A pictorial representation of this process, known as a Feynman diagram, is shown in Fig. 1a. The u and d quarks are ‘first generation’ or lowest mass quarks. Whenever a decay mode is specified in this Letter, the charge conjugate mode is implied.

The B^+ meson is similar to the π^+ , except that the light d antiquark is replaced by the heavy ‘third generation’ (highest mass quarks) beauty (b) antiquark, which has a charge of $+1/3$ and a mass of $\sim 5 \text{ GeV}/c^2$ (about five times the mass of a proton). The decay $B^+ \rightarrow \mu^+ \nu$, represented in Fig. 1b, is allowed but highly suppressed because of angular momentum considerations (helicity suppression) and because it involves transitions between quarks of different generations (CKM suppression), specifically the third and first generations of quarks. All b hadrons, including the B^+ , B_s^0 and B^0 mesons, decay predominantly via the transition of the b antiquark to a ‘second generation’ (intermediate mass quarks) charm (c) antiquark, which is less CKM suppressed, into final states with charmed hadrons. Many allowed decay modes, which typically involve charmed hadrons and other particles, have angular momentum configurations that are not helicity suppressed.

The neutral B_s^0 meson is similar to the B^+ except that the u quark is replaced by a second generation strange (s) quark of charge $-1/3$. The decay of the B_s^0 meson to two muons, shown in Fig. 1c, is forbidden at the elementary level because the Z^0 cannot couple directly to quarks of different flavours, that is, there are no direct ‘flavour changing neutral currents’. However, it is possible to respect this rule and still have this decay occur through ‘higher order’ transitions such as those shown in Fig. 1d and e. These are highly suppressed because each additional interaction vertex reduces their probability of occurring significantly. They are also helicity and CKM suppressed. Consequently, the branching fraction for the $B_s^0 \rightarrow \mu^+ \mu^-$ decay is expected to be very small compared to the dominant b antiquark to c antiquark transitions. The corresponding decay of the B^0 meson, where a d quark replaces the s quark, is even more CKM suppressed because it requires a jump across two quark generations rather than just one.

The branching fractions, \mathcal{B} , of these two decays, accounting for higher-order electromagnetic and strong interaction effects, and using lattice quantum chromodynamics to compute the B_s^0 and B^0 meson decay constants^{5–7}, are reliably calculated¹ in the SM. Their values are $\mathcal{B}(B_s^0 \rightarrow \mu^+ \mu^-)_{\text{SM}} = (3.66 \pm 0.23) \times 10^{-9}$ and $\mathcal{B}(B^0 \rightarrow \mu^+ \mu^-)_{\text{SM}} = (1.06 \pm 0.09) \times 10^{-10}$.

Many theories that seek to go beyond the standard model (BSM) include new phenomena and particles^{8,9}, such as in the diagrams shown in Fig. 1f and g, that can considerably modify the SM branching fractions. In particular, theories with additional Higgs bosons^{10,11} predict possible enhancements to the branching fractions. A significant deviation of either of the two branching fraction measurements from the SM predictions would give insight on how the SM should be extended. Alternatively, a measurement compatible with the SM could provide strong constraints on BSM theories.

*Lists of participants and their affiliations appear in the online version of the paper.

The ratio of the branching fractions of the two decay modes provides powerful discrimination among BSM theories¹². It is predicted in the SM (refs 1, 13 (updates available at <http://itpwiki.unibe.ch/>), 14, 15 (updated results and plots available at <http://www.slac.stanford.edu/xorg/hfag/>)) to be $\mathcal{R} \equiv \mathcal{B}(B^0 \rightarrow \mu^+ \mu^-)_{\text{SM}} / \mathcal{B}(B_s^0 \rightarrow \mu^+ \mu^-)_{\text{SM}} = 0.0295^{+0.0028}_{-0.0025}$. Notably, BSM theories with the property of minimal flavour violation¹⁶ predict the same value as the SM for this ratio.

The first evidence for the decay $B_s^0 \rightarrow \mu^+ \mu^-$ was presented by the LHCb collaboration in 2012¹⁷. Both CMS and LHCb later published results from all data collected in proton–proton collisions at centre-of-mass energies of 7 TeV in 2011 and 8 TeV in 2012. The measurements had comparable precision and were in good agreement^{18,19}, although neither of the individual results had sufficient precision to constitute the first definitive observation of the B_s^0 decay to two muons.

In this Letter, the two sets of data are combined and analysed simultaneously to exploit fully the statistical power of the data and to account for the main correlations between them. The data correspond to total integrated luminosities of 25 fb^{-1} and 3 fb^{-1} for the CMS and LHCb experiments, respectively, equivalent to a total of approximately 10^{12} B_s^0 and B^0 mesons produced in the two experiments together. Assuming the branching fractions given by the SM and accounting for the detection efficiencies, the predicted numbers of decays to be observed in the two experiments together are about 100 for $B_s^0 \rightarrow \mu^+ \mu^-$ and 10 for $B^0 \rightarrow \mu^+ \mu^-$.

The CMS²⁰ and LHCb²¹ detectors are designed to measure SM phenomena with high precision and search for possible deviations. The two collaborations use different and complementary strategies. In addition to performing a broad range of precision tests of the SM and studying the newly-discovered Higgs boson^{22,23}, CMS is designed to search for and study new particles with masses from about $100 \text{ GeV}/c^2$ to a few TeV/c^2 . Since many of these new particles would be able to decay into b quarks and many of the SM measurements also involve b quarks, the detection of b -hadron decays was a key element in the design of CMS. The LHCb collaboration has optimized its detector to study matter–antimatter asymmetries and rare decays of particles containing b quarks, aiming to detect deviations from precise SM predictions that would indicate BSM effects. These different approaches, reflected in the design of the detectors, lead to instrumentation of complementary angular regions with respect to the LHC beams, to operation at different proton–proton collision rates, and to selection of b quark events with different efficiency (for experimental details, see Methods). In general, CMS operates at a higher instantaneous luminosity than LHCb but has a lower efficiency for reconstructing low-mass particles, resulting in a similar sensitivity to LHCb for B^0 or B_s^0 (denoted hereafter by $B_{(s)}^0$) mesons decaying into two muons.

Muons do not have strong nuclear interactions and are too massive to emit a substantial fraction of their energy by electromagnetic

radiation. This gives them the unique ability to penetrate dense materials, such as steel, and register signals in detectors embedded deep within them. Both experiments use this characteristic to identify muons.

The experiments follow similar data analysis strategies. Decays compatible with $B_{(s)}^0 \rightarrow \mu^+ \mu^-$ (candidate decays) are found by combining the reconstructed trajectories (tracks) of oppositely charged particles identified as muons. The separation between genuine $B_{(s)}^0 \rightarrow \mu^+ \mu^-$ decays and random combinations of two muons (combinatorial background), most often from semi-leptonic decays of two different b hadrons, is achieved using the dimuon invariant mass, $m_{\mu^+ \mu^-}$, and the established characteristics of $B_{(s)}^0$ -meson production. For example, because of their lifetimes of about 1.5 ps and their production at the LHC with momenta between a few GeV/c and $\sim 100 \text{ GeV}/c$, $B_{(s)}^0$ mesons travel up to a few centimetres before they decay. Therefore, the $B_{(s)}^0 \rightarrow \mu^+ \mu^-$ ‘decay vertex’, from which the muons originate, is required to be displaced with respect to the ‘production vertex’, the point where the two protons collide. Furthermore, the negative of the $B_{(s)}^0$ candidate’s momentum vector is required to point back to the production vertex.

These criteria, amongst others that have some ability to distinguish known signal events from background events, are combined into boosted decision trees (BDTs)^{24–26}. A BDT is an ensemble of decision trees each placing different selection requirements on the individual variables to achieve the best discrimination between ‘signal-like’ and ‘background-like’ events. Both experiments evaluated many variables for their discriminating power and each chose the best set of about ten to be used in its respective BDT. These include variables related to the quality of the reconstructed tracks of the muons; kinematic variables such as transverse momentum (with respect to the beam axis) of the individual muons and of the $B_{(s)}^0$ candidate; variables related to the decay vertex topology and fit quality, such as candidate decay length; and isolation variables, which measure the activity in terms of other particles in the vicinity of the two muons or their displaced vertex. A BDT must be ‘trained’ on collections of known background and signal events to generate the selection requirements on the variables and the weights for each tree. In the case of CMS, the background events used in the training are taken from intervals of dimuon mass above and below the signal region in data, while simulated events are used for the signal. The data are divided into disjoint sub-samples and the BDT trained on one sub-sample is applied to a different sub-sample to avoid any bias. LHCb uses simulated events for background and signal in the training of its BDT. After training, the relevant BDT is applied to each event in the data, returning a single value for the event, with high values being more signal-like. To avoid possible biases, both experiments kept the small mass interval that includes both the B_s^0 and B^0 signals blind until all selection criteria were established.

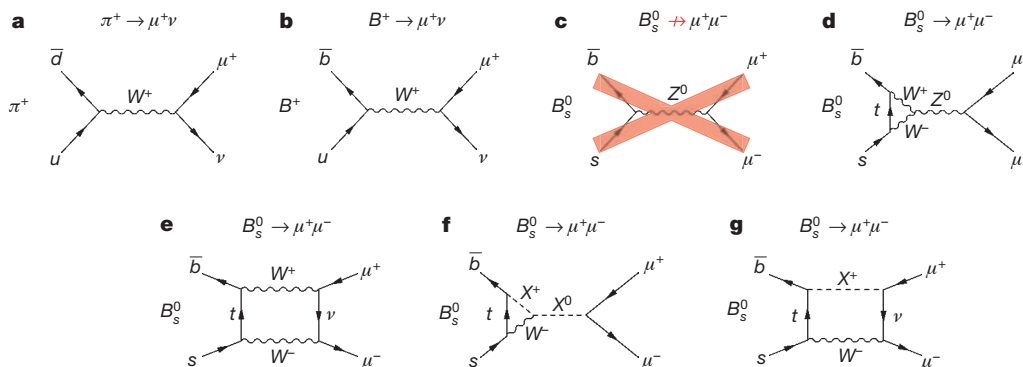


Figure 1 | Feynman diagrams related to the $B_s^0 \rightarrow \mu^+ \mu^-$ decay. **a**, π^+ meson decay through the charged-current process; **b**, B^+ meson decay through the charged-current process; **c**, a B_s^0 decay through the direct flavour changing neutral current process, which is forbidden in the SM, as indicated by a large red

‘X’; **d**, **e**, higher-order flavour changing neutral current processes for the $B_s^0 \rightarrow \mu^+ \mu^-$ decay allowed in the SM; and **f** and **g**, examples of processes for the same decay in theories extending the SM, where new particles, denoted X^0 and X^+ , can alter the decay rate.

In addition to the combinatorial background, specific b -hadron decays, such as $B^0 \rightarrow \pi^- \mu^+ \nu$ where the neutrino cannot be detected and the charged pion is misidentified as a muon, or $B^0 \rightarrow \pi^0 \mu^+ \mu^-$, where the neutral pion in the decay is not reconstructed, can mimic the dimuon decay of the $B_{(s)}^0$ mesons. The invariant mass of the reconstructed dimuon candidate for these processes (semi-leptonic background) is usually smaller than the mass of the $B_{(s)}^0$ or B^0 meson because the neutrino or another particle is not detected. There is also a background component from hadronic two-body $B_{(s)}^0$ decays (peaking background) as $B^0 \rightarrow K^+ \pi^-$, when both hadrons from the decay are misidentified as muons. These misidentified decays can produce peaks in the dimuon invariant-mass spectrum near the expected signal, especially for the $B^0 \rightarrow \mu^+ \mu^-$ decay. Particle identification algorithms are used to minimize the probability that pions and kaons are misidentified as muons, and thus suppress these background sources. Excellent mass resolution is mandatory for distinguishing between B^0 and B_s^0 mesons with a mass difference of about $87 \text{ MeV}/c^2$ and for separating them from backgrounds. The mass resolution for $B_s^0 \rightarrow \mu^+ \mu^-$ decays in CMS ranges from 32 to $75 \text{ MeV}/c^2$, depending on the direction of the muons relative to the beam axis, while LHCb achieves a uniform mass resolution of about $25 \text{ MeV}/c^2$.

The CMS and LHCb data are combined by fitting a common value for each branching fraction to the data from both experiments. The branching fractions are determined from the observed numbers, efficiency-corrected, of $B_{(s)}^0$ mesons that decay into two muons and the total numbers of $B_{(s)}^0$ mesons produced. Both experiments derive the latter from the number of observed $B^+ \rightarrow J/\psi K^+$ decays, whose branching fraction has been precisely measured elsewhere¹⁴. Assuming equal rates for B^+ and B^0 production, this gives the normalization for $B^0 \rightarrow \mu^+ \mu^-$. To derive the number of B_s^0 mesons from this B^+ decay mode, the ratio of b quarks that form (hadronize into) B^+ mesons to those that form B_s^0 mesons is also needed. Measurements of this ratio^{27,28}, for which there is additional discussion in Methods, and of the branching fraction $\mathcal{B}(B^+ \rightarrow J/\psi K^+)$ are used to normalize both sets of data and are constrained within Gaussian uncertainties in the fit. The use of these two results by both CMS and LHCb is the only significant source of correlation between their individual branching fraction measurements. The combined fit takes advantage of the larger data sample to increase the precision while properly accounting for the correlation.

In the simultaneous fit to both the CMS and LHCb data, the branching fractions of the two signal channels are common parameters of interest and are free to vary. Other parameters in the fit are considered as nuisance parameters. Those for which additional knowledge is available are constrained to be near their estimated values by using Gaussian penalties with their estimated uncertainties while the others are free to float in the fit. The ratio of the hadronization probability into B^+ and B_s^0 mesons and the branching fraction of the normalization channel $B^+ \rightarrow J/\psi K^+$ are common, constrained parameters. Candidate decays are categorized according to whether they were detected in CMS or LHCb and to the value of the relevant BDT discriminant. In the case of CMS, they are further categorized according to the data-taking period, and, because of the large variation in mass resolution with angle, whether the muons are both produced at large angles relative to the proton beams (central-region) or at least one muon is emitted at small angle relative to the beams (forward-region). An unbinned extended maximum likelihood fit to the dimuon invariant-mass distribution, in a region of about $\pm 500 \text{ MeV}/c^2$ around the B_s^0 mass, is performed simultaneously in all categories (12 categories from CMS and eight from LHCb). Likelihood contours in the plane of the parameters of interest, $\mathcal{B}(B^0 \rightarrow \mu^+ \mu^-)$ versus $\mathcal{B}(B_s^0 \rightarrow \mu^+ \mu^-)$, are obtained by constructing the test statistic $-2\Delta \ln L$ from the difference in log-likelihood ($\ln L$) values between fits with fixed values for the parameters of interest and the nominal fit. For each of the two branching fractions, a one-dimensional profile likelihood scan is likewise obtained by fixing only the single parameter of interest and allowing the other to vary during the fits. Additional fits are performed where the parameters under consideration are the ratio of the branching fractions relative to their SM predictions, $S_{\text{SM}}^{B_{(s)}^0} \equiv \mathcal{B}(B_{(s)}^0 \rightarrow \mu^+ \mu^-) / \mathcal{B}(B_{(s)}^0 \rightarrow \mu^+ \mu^-)_{\text{SM}}$, or the ratio \mathcal{R} of the two branching fractions.

The combined fit result is shown for all 20 categories in Extended Data Fig. 1. To represent the result of the fit in a single dimuon invariant-mass spectrum, the mass distributions of all categories, weighted according to values of $S/(S+B)$, where S is the expected number of B_s^0 signals and B is the number of background events under the B_s^0 peak in that category, are added together and shown in Fig. 2. The result of the simultaneous fit is overlaid. An alternative representation of the fit to the dimuon invariant-mass distribution for the six

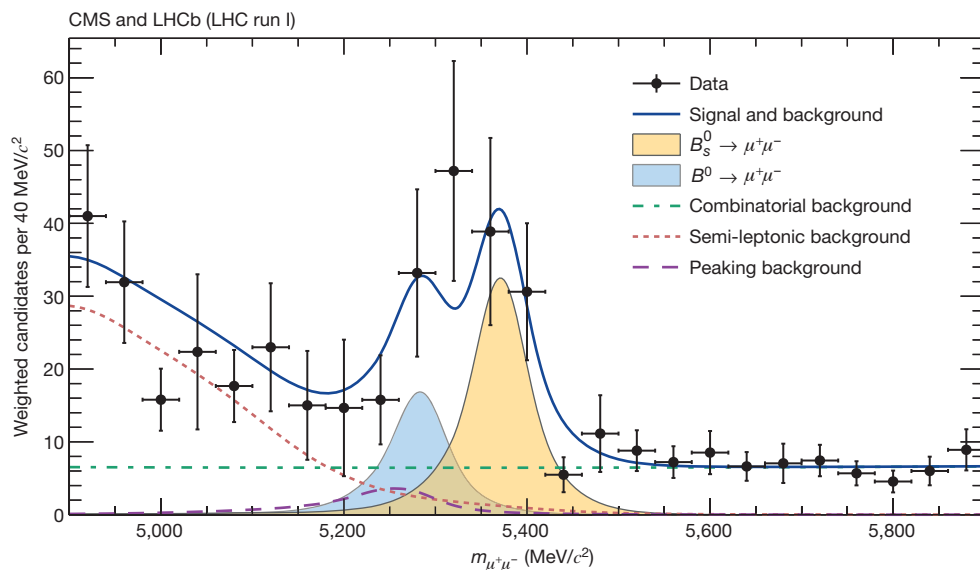


Figure 2 | Weighted distribution of the dimuon invariant mass, $m_{\mu^+\mu^-}$, for all categories. Superimposed on the data points in black are the combined fit (solid blue line) and its components: the B_s^0 (yellow shaded area) and B^0 (light-blue shaded area) signal components; the combinatorial background (dashed green line); the sum of the semi-leptonic backgrounds (dotted salmon

line); and the peaking backgrounds (dashed violet line). The horizontal bar on each histogram point denotes the size of the binning, while the vertical bar denotes the 68% confidence interval. See main text for details on the weighting procedure.

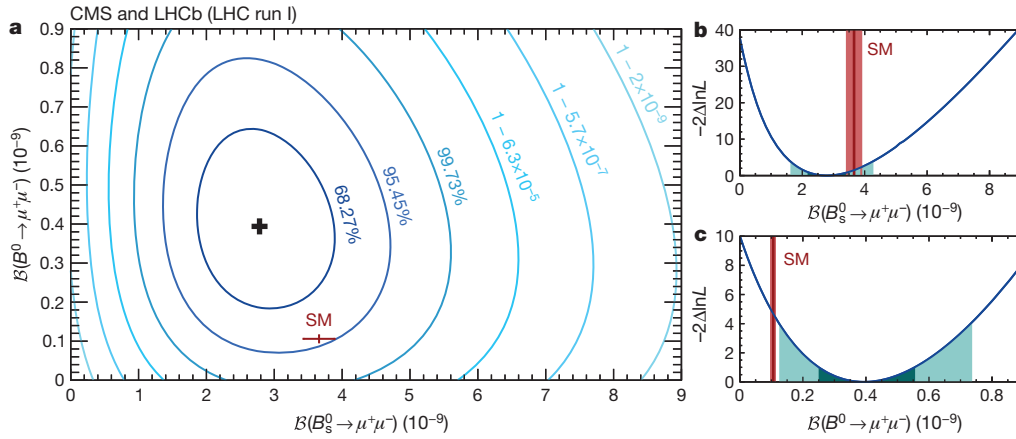


Figure 3 | Likelihood contours in the $\mathcal{B}(B^0 \rightarrow \mu^+ \mu^-)$ versus $\mathcal{B}(B_s^0 \rightarrow \mu^+ \mu^-)$ plane. The (black) cross in **a** marks the best-fit central value. The SM expectation and its uncertainty is shown as the (red) marker. Each contour encloses a region approximately corresponding to the reported confidence level. **b**, **c**, Variations of the test statistic $-2\Delta\ln L$ for $\mathcal{B}(B_s^0 \rightarrow \mu^+ \mu^-)$

categories with the highest $S/(S+B)$ value for CMS and LHCb, as well as displays of events with high probability to be genuine signal decays, are shown in Extended Data Figs 2–4.

The combined fit leads to the measurements $\mathcal{B}(B_s^0 \rightarrow \mu^+ \mu^-) = (2.8^{+0.7}_{-0.6}) \times 10^{-9}$ and $\mathcal{B}(B^0 \rightarrow \mu^+ \mu^-) = (3.9^{+1.6}_{-1.4}) \times 10^{-10}$, where the uncertainties include both statistical and systematic sources, the latter contributing 35% and 18% of the total uncertainty for the B_s^0 and B^0 signals, respectively. Using Wilks' theorem²⁹, the statistical significance in unit of standard deviations, σ , is computed to be 6.2 for the $B_s^0 \rightarrow \mu^+ \mu^-$ decay mode and 3.2 for the $B^0 \rightarrow \mu^+ \mu^-$ mode. For each signal the null hypothesis that is used to compute the significance includes all background components predicted by the SM as well as the other signal, whose branching fraction is allowed to vary freely. The median expected significances assuming the SM branching fractions are 7.4σ and 0.8σ for the B_s^0 and B^0 modes, respectively. Likelihood contours for $\mathcal{B}(B^0 \rightarrow \mu^+ \mu^-)$ versus $\mathcal{B}(B_s^0 \rightarrow \mu^+ \mu^-)$ are shown in Fig. 3. One-dimensional likelihood scans for both decay modes are displayed in the same figure. In addition to the likelihood scan, the statistical significance and confidence intervals for the B^0 branching fraction are determined using simulated experiments. This determination yields a significance of 3.0σ for a B^0 signal with respect to the same null hypothesis described above. Following the Feldman–Cousins³⁰ procedure,

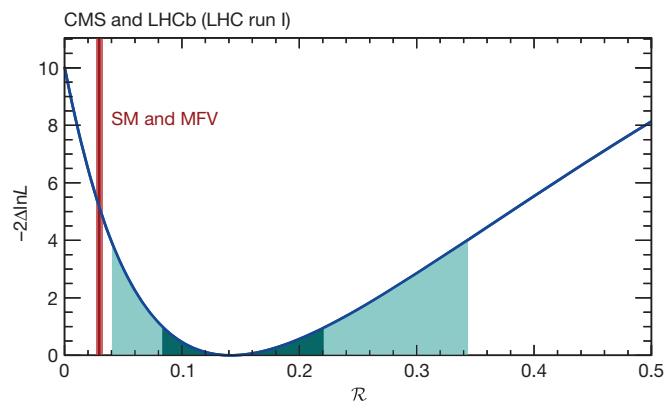


Figure 4 | Variation of the test statistic $-2\Delta\ln L$ as a function of the ratio of branching fractions $\mathcal{R} \equiv \mathcal{B}(B^0 \rightarrow \mu^+ \mu^-)/\mathcal{B}(B_s^0 \rightarrow \mu^+ \mu^-)$. The dark and light (cyan) areas define the $\pm 1\sigma$ and $\pm 2\sigma$ confidence intervals for \mathcal{R} , respectively. The value and uncertainty for \mathcal{R} predicted in the SM, which is the same in BSM theories with the minimal flavour violation (MFV) property, is denoted with the vertical (red) band.

(b) and $\mathcal{B}(B^0 \rightarrow \mu^+ \mu^-)$ (c). The dark and light (cyan) areas define the $\pm 1\sigma$ and $\pm 2\sigma$ confidence intervals for the branching fraction, respectively. The SM prediction and its uncertainty for each branching fraction is denoted with the vertical (red) band.

$\pm 1\sigma$ and $\pm 2\sigma$ confidence intervals for $\mathcal{B}(B^0 \rightarrow \mu^+ \mu^-)$ of $[2.5, 5.6] \times 10^{-10}$ and $[1.4, 7.4] \times 10^{-10}$ are obtained, respectively (see Extended Data Fig. 5).

The fit for the ratios of the branching fractions relative to their SM predictions yields $\mathcal{S}_{SM}^{B_s^0} = 0.76^{+0.20}_{-0.18}$ and $\mathcal{S}_{SM}^{B^0} = 3.7^{+1.6}_{-1.4}$. Associated likelihood contours and one-dimensional likelihood scans are shown in Extended Data Fig. 6. The measurements are compatible with the SM branching fractions of the $B_s^0 \rightarrow \mu^+ \mu^-$ and $B^0 \rightarrow \mu^+ \mu^-$ decays at the 1.2σ and 2.2σ level, respectively, when computed from the one-dimensional hypothesis tests. Finally, the fit for the ratio of branching fractions yields $\mathcal{R} = 0.14^{+0.08}_{-0.06}$, which is compatible with the SM at the 2.3σ level. The one-dimensional likelihood scan for this parameter is shown in Fig. 4.

The combined analysis of data from CMS and LHCb, taking advantage of their full statistical power, establishes conclusively the existence of the $B_s^0 \rightarrow \mu^+ \mu^-$ decay and provides an improved measurement of its branching fraction. This concludes a search that started more than three decades ago (see Extended Data Fig. 7), and initiates a phase of precision measurements of the properties of this decay. It also produces three standard deviation evidence for the $B^0 \rightarrow \mu^+ \mu^-$ decay. The measured branching fractions of both decays are compatible with SM predictions. This is the first time that the CMS and LHCb collaborations have performed a combined analysis of sets of their data in order to obtain a statistically significant observation.

Online Content Methods, along with any additional Extended Data display items and Source Data, are available in the online version of the paper; references unique to these sections appear only in the online paper.

Received 12 November 2014; accepted 31 March 2015.

Published online 13 May 2015.

- Bobeth, C. *et al.* $B_{s,d} \rightarrow l^+ l^-$ in the Standard Model with reduced theoretical uncertainty. *Phys. Rev. Lett.* **112**, 101801 (2014).
- Evans, L. & Bryant, P. LHC machine. *J. Instrum.* **3**, S08001 (2008).
- Planck Collaboration, Ade P. A. R. *et al.* Planck 2013 results. XVI. Cosmological parameters. *Astron. Astrophys.* **571**, A16 (2014).
- Gavela, M., Lozano, M., Orloff, J. & Pène, O. Standard model CP-violation and baryon asymmetry (I). Zero temperature. *Nucl. Phys. B* **430**, 345–381 (1994).
- RBC–UKQCD Collaborations, Witzel, O. B -meson decay constants with domain-wall light quarks and nonperturbatively tuned relativistic b -quarks. Preprint at <http://arxiv.org/abs/1311.0276> (2013).
- HPQCD Collaboration, Na, H. *et al.* B and B_s meson decay constants from lattice QCD. *Phys. Rev. D* **86**, 034506 (2012).
- Fermilab Lattice and MILC Collaborations, Bazavov A. *et al.* B - and D -meson decay constants from three-flavor lattice QCD. *Phys. Rev. D* **85**, 114506 (2012).
- Huang, C.-S., Liao, W. & Yan, Q.-S. The promising process to distinguish supersymmetric models with large $\tan\beta$ from the standard model: $B \rightarrow X_{sl} \mu^+ \mu^-$. *Phys. Rev. D* **59**, 011701 (1998).

9. Rai Choudhury, S. & Gaur, N. Dileptonic decay of B_s meson in SUSY models with large $\tan \beta$. *Phys. Lett. B* **451**, 86–92 (1999).
10. Babu, K. & Kolda, C. F. Higgs-mediated $B^0 \rightarrow \mu^+ \mu^-$ in minimal supersymmetry. *Phys. Rev. Lett.* **84**, 228–231 (2000).
11. Bobeth, C., Ewerth, T., Kruger, F. & Urban, J. Analysis of neutral Higgs-boson contributions to the decays $\bar{B}_s \rightarrow \ell^+ \ell^-$ and $B \rightarrow K \ell^+ \ell^-$. *Phys. Rev. D* **64**, 074014 (2001).
12. Buras, A. J. Relations between $\Delta M_{s,d}$ and $B_{s,d} \rightarrow \mu \bar{\mu}$ in models with minimal flavor violation. *Phys. Lett. B* **566**, 115–119 (2003).
13. Aoki, S. *et al.* Review of lattice results concerning low-energy particle physics. *Eur. Phys. J. C* **74**, 2890 (2014).
14. Particle Data Group, Beringer, J. *et al.* Review of particle physics. *Phys. Rev. D* **86**, 010001 (2012); 2013 partial update for the 2014 edition at <http://pdg.lbl.gov>.
15. Heavy Flavor Averaging Group, Amhis, Y. *et al.* Averages of b -hadron, c -hadron, and τ -lepton properties as of early 2012. Preprint at <http://arXiv.org/abs/1207.1158> (2012).
16. D'Ambrosio, G., Giudice, G. F., Isidori, G. & Strumia, A. Minimal flavour violation: an effective field theory approach. *Nucl. Phys. B* **645**, 155–187 (2002).
17. LHCb Collaboration, Aaij, R. *et al.* First evidence for the decay $B_s^0 \rightarrow \mu^+ \mu^-$. *Phys. Rev. Lett.* **110**, 021801 (2013).
18. CMS Collaboration, Chatrchyan, S. *et al.* Measurement of the $B_s^0 \rightarrow \mu^+ \mu^-$ branching fraction and search for $B^0 \rightarrow \mu^+ \mu^-$ with the CMS experiment. *Phys. Rev. Lett.* **111**, 101804 (2013).
19. LHCb Collaboration, Aaij, R. *et al.* Measurement of the $B_s^0 \rightarrow \mu^+ \mu^-$ branching fraction and search for $B^0 \rightarrow \mu^+ \mu^-$ decays at the LHCb experiment. *Phys. Rev. Lett.* **111**, 101805 (2013).
20. CMS Collaboration, Chatrchyan, S. *et al.* The CMS experiment at the CERN LHC. *J. Instrum.* **3**, S08004 (2008).
21. LHCb Collaboration, Alves, A. A. Jr *et al.* The LHCb detector at the LHC. *J. Instrum.* **3**, S08005 (2008).
22. ATLAS Collaboration, Aad, G. *et al.* Observation of a new particle in the search for the Standard Model Higgs boson with the ATLAS detector at the LHC. *Phys. Lett. B* **716**, 1–29 (2012).
23. CMS Collaboration, Chatrchyan, S. *et al.* Observation of a new boson at a mass of 125 GeV with the CMS experiment at the LHC. *Phys. Lett. B* **716**, 30–61 (2012).
24. Breiman, L., Friedman, J. H., Olshen, R. A. & Stone, C. J. *Classification and Regression Trees* (Wadsworth International Group, 1984).
25. Freund, Y. & Schapire, R. E. A decision-theoretic generalization of on-line learning and an application to boosting. *J. Comput. Syst. Sci.* **55**, 119–139 (1997).
26. Hoecker, A. *et al.* TMVA: Toolkit for Multivariate Data Analysis. *Proc. Sci. Adv. Comput. Anal. Techn. Phys. Res.* 040 http://pos.sissa.it/archive/conferences/050/040/ACAT_040.pdf (2007).
27. LHCb Collaboration, Aaij, R. *et al.* Measurement of b hadron production fractions in 7 TeV pp collisions. *Phys. Rev. D* **85**, 032008 (2012).
28. LHCb Collaboration, Aaij, R. *et al.* Measurement of the fragmentation fraction ratio f_s^b/f_d and its dependence on B meson kinematics. *J. High Energy Phys.* **4**, 1 (2013); updated in <https://cds.cern.ch/record/1559262/files/LHCb-CONF-2013-011.pdf>.
29. Wilks, S. S. The large-sample distribution of the likelihood ratio for testing composite hypotheses. *Ann. Math. Stat.* **9**, 60–62 (1938).
30. Feldman, G. J. & Cousins, R. D. Unified approach to the classical statistical analysis of small signals. *Phys. Rev. D* **57**, 3873–3889 (1998).

Acknowledgements We express our gratitude to colleagues in the CERN accelerator departments for the excellent performance of the LHC. We thank the technical and administrative staff at CERN, at the CMS institutes and at the LHCb institutes. In addition, we gratefully acknowledge the computing centres and personnel of the Worldwide LHC Computing Grid for delivering so effectively the computing infrastructure essential to our analyses. Finally, we acknowledge the enduring support

for the construction and operation of the LHC, the CMS and the LHCb detectors provided by CERN and by many funding agencies. The following agencies provide support for both CMS and LHCb: CAPES, CNPq, FAPERJ and FINEP (Brazil); NSFC (China); CNRS/IN2P3 (France); BMBF, DFG and HGF (Germany); SFI (Ireland); INFN (Italy); NASU (Ukraine); STFC (UK); and NSF (USA). Agencies that provide support for CMS only are BMWFW and FWF (Austria); FNRS and FWO (Belgium); FAPESP (Brazil); MES (Bulgaria); CAS and MoST (China); COLCIENCIAS (Colombia); MSES and CSF (Croatia); RPF (Cyprus); MoER, ERC IUT and ERDF (Estonia); Academy of Finland, MEC, and HIP (Finland); CEA (France); GSRT (Greece); OTKA and NIH (Hungary); DAE and DST (India); IPM (Iran); NRF and WCU (Republic of Korea); LAS (Lithuania); MOE and UM (Malaysia); CINVESTAV, CONACYT, SEP, and UASLP-FAI (Mexico); MBIE (New Zealand); PAEC (Pakistan); MSHE and NSC (Poland); FCT (Portugal); JINR (Dubna); MON, RosAtom, RAS and RFBR (Russia); MESTD (Serbia); SEIDI and CPAN (Spain); Swiss Funding Agencies (Switzerland); MST (Taipei); ThEPCenter, IPST, STAR and NSTDA (Thailand); TUBITAK and TAEK (Turkey); SFFR (Ukraine); and DOE (USA). Agencies that provide support for only LHCb are: FINEP (Brazil); MPG (Germany); FOM and NWO (The Netherlands); MNIW and NCN (Poland); MEN/IFA (Romania); MinES and FANO (Russia); MinEco (Spain); SNSF and SER (Switzerland). Individuals from the CMS collaboration have received support from the Marie-Curie programme and the European Research Council and EPLANET (European Union); the Leventis Foundation; the A. P. Sloan Foundation; the Alexander von Humboldt Foundation; the Belgian Federal Science Policy Office; the Fonds pour la Formation à la Recherche dans l'Industrie et dans l'Agriculture (FRIABelgium); the Agentschap voor Innovatie door Wetenschap en Technologie (IWT-Belgium); the Ministry of Education, Youth and Sports (MEYS) of the Czech Republic; the Council of Science and Industrial Research, India; the HOMING PLUS programme of Foundation for Polish Science, cofinanced from European Union, Regional Development Fund; the Compagnia di San Paolo (Torino); the Consorzio per la Fisica (Trieste); MIUR project 20108T4XTM (Italy); the Thalis and Aristeia programmes cofinanced by EU-ESF and the Greek NSRF; and the National Priorities Research Program by Qatar National Research Fund. Individual groups or members of the LHCb collaboration have received support from EPLANET, Marie Skłodowska-Curie Actions and ERC (European Union), Conseil général de Haute-Savoie, Labex ENIGMASS and OCEVU, Région Auvergne (France), RFBR (Russia), XuntaGal and GENCAT (Spain), Royal Society and Royal Commission for the Exhibition of 1851 (UK). LHCb is also thankful for the computing resources and the access to software R&D tools provided by Yandex LLC (Russia). The CMS and LHCb collaborations are indebted to the communities behind the multiple open source software packages on which they depend.

Author Contributions All authors have contributed to the publication, being variously involved in the design and the construction of the detectors, in writing software, calibrating sub-systems, operating the detectors and acquiring data and finally analysing the processed data.

Author Information Reprints and permissions information is available at www.nature.com/reprints. The authors declare no competing financial interests. Readers are welcome to comment on the online version of the paper. Correspondence and requests for materials should be addressed to cms-publication-committee-chair@cern.ch and to lhc-editorial-board-chair@cern.ch.



This work is licensed under a Creative Commons Attribution-NonCommercial-ShareAlike 3.0 Unported licence. The images or other third party material in this article are included in the article's Creative Commons licence, unless indicated otherwise in the credit line; if the material is not included under the Creative Commons licence, users will need to obtain permission from the licence holder to reproduce the material. To view a copy of this licence, visit <http://creativecommons.org/licenses/by-nc-sa/3.0>

METHODS

Experimental setup. At the Large Hadron Collider (LHC), two counter-rotating beams of protons, contained and guided by superconducting magnets spaced around a 27 km circular tunnel, located approximately 100 m underground near Geneva, Switzerland, are brought into collision at four interaction points (IPs). The study presented in this Letter uses data collected at energies of 3.5 TeV per beam in 2011 and 4 TeV per beam in 2012 by the CMS and LHCb experiments located at two of these IPs.

The CMS and LHCb detectors are both designed to look for phenomena beyond the SM (BSM), but using complementary strategies. The CMS detector²⁰, shown in Extended Data Fig. 3, is optimized to search for yet unknown heavy particles, with masses ranging from 100 GeV/ c^2 to a few TeV/ c^2 , which, if observed, would be a direct manifestation of BSM phenomena. Since many of the hypothesized new particles can decay into particles containing b quarks or into muons, CMS is able to detect efficiently and study B^0 (5,280 MeV/ c^2) and B_s^0 (5,367 MeV/ c^2) mesons decaying to two muons even though it is designed to search for particles with much larger masses. The CMS detector covers a very large range of angles and momenta to reconstruct high-mass states efficiently. To that extent, it employs a 13 m long, 6 m diameter superconducting solenoid magnet, operated at a field of 3.8 T, centred on the IP with its axis along the beam direction and covering both hemispheres. A series of silicon tracking layers, consisting of silicon pixel detectors near the beam and silicon strips farther out, organized in concentric cylinders around the beam, extending to a radius of 1.1 m and terminated on each end by planar detectors (disks) perpendicular to the beam, measures the momentum, angles, and position of charged particles emerging from the collisions. Tracking coverage starts from the direction perpendicular to the beam and extends to within 220 mrad from it on both sides of the IP. The inner three cylinders and disks extending from 4.3 to 10.7 cm in radius transverse to the beam are arrays of $100 \times 150 \mu\text{m}^2$ silicon pixels, which can distinguish the displacement of the b -hadron decays from the primary vertex of the collision. The silicon strips, covering radii from 25 cm to approximately 110 cm, have pitches ranging from 80 to 183 μm . The impact parameter is measured with a precision of 10 μm for transverse momenta of 100 GeV/ c and 20 μm for 10 GeV/ c . The momentum resolution, provided mainly by the silicon strips, changes with the angle relative to the beam direction, resulting in a mass resolution for $B_{(s)}^0 \rightarrow \mu^+ \mu^-$ decays that varies from 32 MeV/ c^2 for $B_{(s)}^0$ mesons produced perpendicularly to the proton beams to 75 MeV/ c^2 for those produced at small angles relative to the beam direction. After the tracking system, at a greater distance from the IP, there is a calorimeter that stops (absorbs) all particles except muons and measures their energies. The calorimeter consists of an electromagnetic section followed by a hadronic section. Muons are identified by their ability to penetrate the calorimeter and the steel return yoke of the solenoid magnet and to produce signals in gas-ionization particle detectors located in compartments within the steel yoke. The CMS detector has no capability to discriminate between charged hadron species, pions, kaons, or protons, that is effective at the typical particle momenta in this analysis.

The primary commitment of the LHCb collaboration is the study of particle-antiparticle asymmetries and of rare decays of particles containing b and c quarks. LHCb aims at detecting BSM particles indirectly by measuring their effect on b -hadron properties for which precise SM predictions exist. The production cross section of b hadrons at the LHC is particularly large at small angles relative to the colliding beams. The small-angle region also provides advantages for the detection and reconstruction of a wide range of their decays. The LHCb experiment²¹, shown in Extended Data Fig. 4, instruments the angular interval from 10 to 300 mrad with respect to the beam direction on one side of the interaction region. Its detectors are designed to reconstruct efficiently a wide range of b -hadron decays, resulting in charged pions and kaons, protons, muons, electrons, and photons in the final state. The detector includes a high-precision tracking system consisting of a silicon strip vertex detector, a large-area silicon strip detector located upstream of a dipole magnet characterized by a field integral of 4 T m, and three stations of silicon strip detectors and straw drift tubes downstream of the magnet. The vertex detector has sufficient spatial resolution to distinguish the slight displacement of the weakly decaying b hadron from the primary production vertex where the two protons collided and produced it. The tracking detectors upstream and downstream of the dipole magnet measure the momenta of charged particles. The combined tracking system provides a momentum measurement with an uncertainty that varies from 0.4% at 5 GeV/ c to 0.6% at 100 GeV/ c . This results in an invariant-mass resolution of 25 MeV/ c^2 for $B_{(s)}^0$ mesons decaying to two muons that is nearly independent of the angle with respect to the beam. The impact parameter resolution is smaller than 20 μm for particle tracks with large transverse momentum. Different types of charged hadrons are distinguished by information from two ring-imaging Cherenkov detectors. Photon, electron, and hadron candidates are identified by calorimeters. Muons are identified by a system composed of alternating layers of iron and multiwire proportional chambers.

Neither CMS nor LHCb records all the interactions occurring at its IP because the data storage and analysis costs would be prohibitive. Since most of the interactions are reasonably well characterized (and can be further studied by recording only a small sample of them) specific event filters (known as triggers) select the rare processes that are of interest to the experiments. Both CMS and LHCb implement triggers that specifically select events containing two muons. The triggers of both experiments have a hardware stage, based on information from the calorimeter and muon systems, followed by a software stage, consisting of a large computing cluster that uses all the information from the detector, including the tracking, to make the final selection of events to be recorded for subsequent analysis. Since CMS is designed to look for much heavier objects than $B_{(s)}^0$ mesons, it selects events that contain muons with higher transverse momenta than those selected by LHCb. This eliminates many of the $B_{(s)}^0$ decays while permitting CMS to run at a higher proton-proton collision rate to look for the more rare massive particles. Thus CMS runs at higher collision rates but with lower efficiency than LHCb for $B_{(s)}^0$ mesons decaying to two muons. The overall sensitivity to these decays turns out to be similar in the two experiments.

CMS and LHCb are not the only collaborations to have searched for $B_{(s)}^0 \rightarrow \mu^+ \mu^-$ and $B^0 \rightarrow \mu^+ \mu^-$ decays. Over three decades, a total of eleven collaborations have taken part in this search¹⁴, as illustrated by Extended Data Fig. 7. This plot gathers the results from CLEO^{21–25}, ARGUS²⁶, UA1^{27,28}, CDF^{29–44}, L3⁴⁵, DØ^{46–50}, Belle⁵¹, Babar^{52,53}, LHCb^{17,54–57}, CMS^{18,58,59} and ATLAS⁶⁰.

Analysis description. The analysis techniques used to obtain the results presented in this Letter are very similar to those used to obtain the individual result in each collaboration, described in more detail in refs 18, 19. Here only the main analysis steps are reviewed and the changes used in the combined analysis are highlighted. Data samples for this analysis were collected by the two experiments in proton-proton collisions at a centre-of-mass energy of 7 and 8 TeV during 2011 and 2012, respectively. These samples correspond to a total integrated luminosity of 25 and 3 fb⁻¹ for the CMS and LHCb experiments, respectively, and represent their complete data sets from the first running period of the LHC.

The trigger criteria were slightly different between the two experiments. The large majority of events were triggered by requirements on one or both muons of the signal decay: the LHCb detector triggered on muons with transverse momentum $p_T > 1.5$ GeV/ c while the CMS detector, because of its geometry and higher instantaneous luminosity, triggered on two muons with $p_T > 4$ (3) GeV/ c for the leading (sub-leading) muon.

The data analysis procedures in the two experiments follow similar strategies. Pairs of high-quality oppositely charged particle tracks that have one of the expected patterns of hits in the muon detectors are fitted to form a common vertex in three dimensions, which is required to be displaced from the primary interaction vertex (PV) and to have a small χ^2 in the fit. The resulting $B_{(s)}^0$ candidate is further required to point back to the PV, for example, to have a small impact parameter, consistent with zero, with respect to it. The final classification of data events is done in categories of the response of a multivariate discriminant (MVA) combining information from the kinematics and vertex topology of the events. The type of MVA used is a boosted decision tree (BDT)^{24–26}. The branching fractions are then obtained by a fit to the dimuon invariant mass, $m_{\mu^+ \mu^-}$, of all categories simultaneously.

The signals appear as peaks at the B_s^0 and B^0 masses in the invariant-mass distributions, observed over background events. One of the components of the background is combinatorial in nature, as it is due to the random combinations of genuine muons. These produce a smooth dimuon mass distribution in the vicinity of the B_s^0 and B^0 masses, estimated in the fit to the data by extrapolation from the sidebands of the invariant-mass distribution. In addition to the combinatorial background, certain specific b -hadron decays can mimic the signal or contribute to the background in its vicinity. In particular, the semi-leptonic decays $B^0 \rightarrow \pi^- \mu^+ \nu$, $B_s^0 \rightarrow K^- \mu^+ \nu$, and $A_b^0 \rightarrow p \mu^- \bar{\nu}$ can have reconstructed masses that are near the signal if one of the hadrons is misidentified as a muon and is combined with a genuine muon. Similarly the dimuon coming from the rare $B^0 \rightarrow \pi^0 \mu^+ \mu^-$ and $B^+ \rightarrow \pi^+ \mu^+ \mu^-$ decays can also fake the signal. All these background decays, when reconstructed as a dimuon final state, have invariant masses that are lower than the masses of the B^0 and B_s^0 mesons, because they are missing one of the original decay particles. An exception is the decay $A_b^0 \rightarrow p \mu^- \bar{\nu}$, which can also populate, with a smooth mass distribution, higher-mass regions. Furthermore, background due to misidentified hadronic two-body decays $B_{(s)}^0 \rightarrow h^+ h'^-$, where $h^{(\prime)} = \pi$ or K , is present when both hadrons are misidentified as muons. These misidentified decays produce an apparent dimuon invariant-mass peak close to the B^0 mass value. Such a peak can mimic a $B^0 \rightarrow \mu^+ \mu^-$ signal and is estimated from control channels and added to the fit.

The distributions of signal in the invariant mass and in the MVA discriminant are derived from simulations with a detailed description of the detector response

for CMS and are calibrated using exclusive two-body hadronic decays in data for LHCb. The distributions for the backgrounds are obtained from simulation with the exception of the combinatorial background. The latter is obtained by interpolating from the data invariant-mass sidebands separately for each category, after the subtraction of the other background components.

To compute the signal branching fractions, the numbers of B_s^0 and B^0 mesons that are produced, as well as the numbers of those that have decayed into a dimuon pair, are needed. The latter numbers are the raw results of this analysis, whereas the former need to be determined from measurements of one or more ‘normalization’ decay channels, which are abundantly produced, have an absolute branching fraction that is already known with good precision, and that share characteristics with the signals, so that their trigger and selection efficiencies do not differ significantly. Both experiments use the $B^+ \rightarrow J/\psi K^+$ decay as a normalization channel with $\mathcal{B}(B^+ \rightarrow J/\psi(\mu^+\mu^-)K^+) = (6.10 \pm 0.19) \times 10^{-5}$, and LHCb also uses the $B^0 \rightarrow K^+\pi^-$ channel with $\mathcal{B}(B^0 \rightarrow K^+\pi^-) = (1.96 \pm 0.05) \times 10^{-5}$. Both branching fraction values are taken from ref. 14. Hence, the $B_s^0 \rightarrow \mu^+\mu^-$ branching fraction is expressed as a function of the number of signal events ($N_{B_s^0 \rightarrow \mu^+\mu^-}$) in the data normalized to the numbers of $B^+ \rightarrow J/\psi K^+$ and $B^0 \rightarrow K^+\pi^-$ events:

$$\mathcal{B}(B_s^0 \rightarrow \mu^+\mu^-) = \frac{N_{B_s^0 \rightarrow \mu^+\mu^-}}{N_{\text{norm.}}} \times \frac{f_d}{f_s} \times \frac{\varepsilon_{\text{norm.}}}{\varepsilon_{B_s^0 \rightarrow \mu^+\mu^-}} \times \mathcal{B}_{\text{norm.}} = \alpha_{\text{norm.}} \times N_{B_s^0 \rightarrow \mu^+\mu^-} \quad (1)$$

where the ‘norm.’ subscript refers to either of the normalization channels. The values of the normalization parameter $\alpha_{\text{norm.}}$ obtained by LHCb from the two normalization channels are found in good agreement and their weighted average is used. In this formula ε indicates the total event detection efficiency including geometrical acceptance, trigger selection, reconstruction, and analysis selection for the corresponding decay. The f_d/f_s factor is the ratio of the probabilities for a b quark to hadronize into a B^0 as compared to a B_s^0 meson; the probability to hadronize into a B^+ (f_u) is assumed to be equal to that into B^0 (f_d) on the basis of theoretical grounds, and this assumption is checked on data. The value of $f_d/f_s = 3.86 \pm 0.22$ measured by LHCb^{27,28,61} is used in this analysis. As the value of f_d/f_s depends on the kinematic range of the considered particles, which differs between LHCb and CMS, CMS checked this observable with the decays $B_s^0 \rightarrow J/\psi\phi$ and $B^+ \rightarrow J/\psi K^+$ within its acceptance, finding a consistent value. An additional systematic uncertainty of 5% was assigned to f_d/f_s to account for the extrapolation of the LHCb result to the CMS acceptance. An analogous formula to that in equation (1) holds for the normalization of the $B^0 \rightarrow \mu^+\mu^-$ decay, with the notable difference that the f_d/f_s factor is replaced by $f_d/f_u = 1$.

The antiparticle \bar{B}^0 (\bar{B}_s^0) and the particle B^0 (B_s^0) can both decay into two muons and no attempt is made in this analysis to determine whether the antiparticle or particle was produced (untagged method). However, the B^0 and B_s^0 particles are known to oscillate, that is to transform continuously into their antiparticles and vice versa. Therefore, a quantum superposition of particle and antiparticle states propagates in the laboratory before decaying. This superposition can be described by two ‘mass eigenstates’, which are symmetric and antisymmetric in the charge-parity (CP) quantum number, and have slightly different masses. In the SM, the heavy eigenstate can decay into two muons, whereas the light eigenstate cannot without violating the CP quantum number conservation. In BSM models, this is not necessarily the case. In addition to their masses, the two eigenstates of the B_s^0 system also differ in their lifetime values¹⁴. The lifetimes of the light and heavy eigenstates are also different from the average B_s^0 lifetime, which is used by CMS and LHCb in the simulations of signal decays. Since the information on the displacement of the secondary decay with respect to the PV is used as a discriminant against combinatorial background in the analysis, the efficiency versus lifetime has a model-dependent bias⁶² that must be removed. This bias is estimated assuming SM dynamics. Owing to the smaller difference between the lifetime of its heavy and light mass eigenstates, no correction is required for the B^0 decay mode.

Detector simulations are needed by both CMS and LHCb. CMS relies on simulated events to determine resolutions and trigger and reconstruction efficiencies, and to provide the signal sample for training the BDT. The dimuon mass resolution given by the simulation is validated using data on J/ψ , Y , and Z -boson decays to two muons. The tracking and trigger efficiencies obtained from the simulation are checked using special control samples from data. The LHCb analysis is designed to minimize the impact of discrepancies between simulations and data. The mass resolution is measured with data. The distribution of the BDT for the signal and for the background is also calibrated with data using control channels and mass sidebands. The efficiency ratio for the trigger is also largely determined from data. The simulations are used to determine the efficiency ratios of selection and reconstruction processes between signal and normalization channels. As for the overall detector simulation, each experiment has a team dedicated to making the simulations as complete and realistic as possible. The simulated data are constantly being compared to the

actual data. Agreement between simulation and data in both experiments is quite good, often extending well beyond the cores of distributions. Differences occur because, for example, of incomplete description of the material of the detectors, approximations made to keep the computer time manageable, residual uncertainties in calibration and alignment, and discrepancies or limitations in the underlying theory and experimental data used to model the relevant collisions and decays. Small differences between simulation and data that are known to have an impact on the result are treated either by reweighting the simulations to match the data or by assigning appropriate systematic uncertainties.

Small changes are made to the analysis procedure with respect to refs 18, 19 in order to achieve a consistent combination between the two experiments. In the LHCb analysis, the $A_b^0 \rightarrow p\mu^-\bar{\nu}$ background component, which was not included in the fit for the previous result but whose effect was accounted for as an additional systematic uncertainty, is now included in the standard fit. The following modifications are made to the CMS analysis: the $A_b^0 \rightarrow p\mu^-\bar{\nu}$ branching fraction is updated to a more recent prediction^{63,64} of $\mathcal{B}(A_b^0 \rightarrow p\mu^-\bar{\nu}) = (4.94 \pm 2.19) \times 10^{-4}$; the phase space model of the decay $A_b^0 \rightarrow p\mu^-\bar{\nu}$ is changed to a more appropriate semileptonic decay model⁶⁵; and the decay time bias correction for the B_s^0 , previously absent from the analysis, is now calculated and applied with a different correction for each category of the multivariate discriminant.

These modifications result in changes in the individual results of each experiment. The modified CMS analysis, applied on the CMS data, yields

$$\mathcal{B}(B_s^0 \rightarrow \mu^+\mu^-) = (2.8_{-0.9}^{+1.1}) \times 10^{-9} \quad \text{and} \quad \mathcal{B}(B^0 \rightarrow \mu^+\mu^-) = (4.4_{-1.9}^{+2.2}) \times 10^{-10} \quad (2)$$

while the LHCb results change to

$$\mathcal{B}(B_s^0 \rightarrow \mu^+\mu^-) = (2.7_{-0.9}^{+1.1}) \times 10^{-9} \quad \text{and} \quad \mathcal{B}(B^0 \rightarrow \mu^+\mu^-) = (3.3_{-2.1}^{+2.4}) \times 10^{-10} \quad (3)$$

These results are only slightly different from the published ones and are in agreement with each other.

Simultaneous fit. The goal of the analysis presented in this Letter is to combine the full data sets of the two experiments to reduce the uncertainties on the branching fractions of the signal decays obtained from the individual determinations. A simultaneous unbinned extended maximum likelihood fit is performed to the data of the two experiments, using the invariant-mass distributions of all 20 MVA discriminant categories of both experiments. The invariant-mass distributions are defined in the dimuon mass ranges $m_{\mu^+\mu^-} \in [4.9, 5.9] \text{ GeV}/c^2$ and $[4.9, 6.0] \text{ GeV}/c^2$ for the CMS and LHCb experiments, respectively. The branching fractions of the signal decays, the hadronization fraction ratio f_d/f_s , and the branching fraction of the normalization channel $B^+ \rightarrow J/\psi K^+$ are treated as common parameters. The value of the $B^+ \rightarrow J/\psi K^+$ branching fraction is the combination of results from five different experiments¹⁴, taking advantage of all their data to achieve the most precise input parameters for this analysis. The combined fit takes advantage of the larger data sample and proper treatment of the correlations between the individual measurements to increase the precision and reliability of the result, respectively.

Fit parameters, other than those of primary physics interest, whose limited knowledge affects the results, are called ‘nuisance parameters’. In particular, systematic uncertainties are modelled by introducing nuisance parameters into the statistical model and allowing them to vary in the fit; those for which additional knowledge is present are constrained using Gaussian distributions. The mean and standard deviation of these distributions are set to the central value and uncertainty obtained either from other measurements or from control channels. The statistical component of the final uncertainty on the branching fractions is obtained by repeating the fit after fixing all of the constrained nuisance parameters to their best fitted values. The systematic component is then calculated by subtracting in quadrature the statistical component from the total uncertainty. In addition to the free fit, a two-dimensional likelihood ratio scan in the plane $\mathcal{B}(B^0 \rightarrow \mu^+\mu^-)$ versus $\mathcal{B}(B_s^0 \rightarrow \mu^+\mu^-)$ is performed.

Feldman–Cousins confidence interval. The Feldman–Cousins likelihood ratio ordering procedure³⁰ is a unified frequentist method to construct single- and double-sided confidence intervals for parameters of a given model adapted to the data. It provides a natural transition between single-sided confidence intervals, used to define upper or lower limits, and double-sided ones. Since the single-experiment results^{18,19} showed that the $B^0 \rightarrow \mu^+\mu^-$ signal is at the edge of the probability region customarily used to assert statistically significant evidence for a result, a Feldman–Cousins procedure is performed. This allows a more reliable determination of the confidence interval and significance of this signal without the assumptions required for the use of Wilks’ theorem. In addition, a prescription for the treatment of nuisance parameters has to be chosen because scanning the whole parameter space in the presence of more than a few parameters is computationally too intensive. In this case the procedure described by the ATLAS and CMS Higgs combination group⁶⁵ is adopted. For each point of the space of the relevant parameters, the nuisance parameters are fixed to their best value estimated by the mean

of a maximum likelihood fit to the data with the value of $\mathcal{B}(B^0 \rightarrow \mu^+ \mu^-)$ fixed and all nuisance parameters profiled with Gaussian penalties. Sampling distributions are constructed for each tested point of the parameter of interest by generating simulated experiments and performing maximum likelihood fits in which the Gaussian mean values of the external constraints on the nuisance parameters are randomized around the best-fit values for the nuisance parameters used to generate the simulated experiments. The sampling distribution is constructed from the distribution of the negative log-likelihood ratio evaluated on the simulated experiments by performing one likelihood fit in which the value of $\mathcal{B}(B^0 \rightarrow \mu^+ \mu^-)$ is free to float and another with the $\mathcal{B}(B^0 \rightarrow \mu^+ \mu^-)$ fixed to the tested point value. This sampling distribution is then converted to a confidence level by evaluating the fraction of simulated experiments entries with a value for the negative log-likelihood ratio greater than or equal to the value observed in the data for each tested point. The results of this procedure are shown in Extended Data Fig. 5.

31. CLEO Collaboration, Giles R. *et al.* Two-body decays of B mesons. *Phys. Rev. D* **30**, 2279–2294 (1984).
32. CLEO Collaboration, Avery P. *et al.* Limits on rare exclusive decays of B mesons. *Phys. Lett. B* **183**, 429–433 (1987).
33. CLEO Collaboration, Avery P. *et al.* A search for exclusive penguin decays of B mesons. *Phys. Lett. B* **223**, 470–475 (1989).
34. CLEO Collaboration, Ammar R. *et al.* Search for B^0 decays to two charged leptons. *Phys. Rev. D* **49**, 5701–5704 (1994).
35. CLEO Collaboration, Bergfeld T. *et al.* Search for decays of B^0 mesons into pairs of leptons: $B^0 \rightarrow e^+ e^-$, $B^0 \rightarrow \mu^+ \mu^-$ and $B^0 \rightarrow e^\pm \mu^\mp$. *Phys. Rev. D* **62**, 091102 (2000).
36. ARGUS Collaboration, Albrecht H. *et al.* B meson decays into charmonium states. *Phys. Lett. B* **199**, 451–456 (1987).
37. UA1 Collaboration, Albajar C. *et al.* Low mass dimuon production at the CERN proton-antiproton collider. *Phys. Lett. B* **209**, 397–406 (1988).
38. UA1 Collaboration, Albajar C. *et al.* A search for rare B meson decays at the CERN Sp \bar{p} S collider. *Phys. Lett. B* **262**, 163–170 (1991).
39. CDF Collaboration, Abe F. *et al.* Search for flavor-changing neutral current B meson decays in $p\bar{p}$ collisions at $\sqrt{s} = 1.8$ TeV. *Phys. Rev. Lett.* **76**, 4675–4680 (1996).
40. CDF Collaboration, Abe F. *et al.* Search for the decays $B_s^0 \rightarrow \mu^+ \mu^-$ and $B_d^0 \rightarrow \mu^+ \mu^-$ in $p\bar{p}$ collisions at $\sqrt{s} = 1.8$ TeV. *Phys. Rev. D* **57**, 3811–3816 (1998).
41. CDF Collaboration, Acosta D. *et al.* Search for $B_s^0 \rightarrow \mu^+ \mu^-$ and $B_d^0 \rightarrow \mu^+ \mu^-$ decays in $p\bar{p}$ collisions at $\sqrt{s} = 1.96$ TeV. *Phys. Rev. Lett.* **93**, 032001 (2004).
42. CDF Collaboration, Abulencia A. *et al.* Search for $B_s \rightarrow \mu^+ \mu^-$ and $B_d \rightarrow \mu^+ \mu^-$ decays in $p\bar{p}$ collisions with CDF II. *Phys. Rev. Lett.* **95**, 221805 (2005).
43. CDF Collaboration, Aaltonen T. *et al.* Search for $B_s \rightarrow \mu^+ \mu^-$ and $B_d \rightarrow \mu^+ \mu^-$ decays with CDF II. *Phys. Rev. Lett.* **107**, 191801 (2011).
44. CDF Collaboration, Aaltonen T. *et al.* Search for $B_s \rightarrow \mu^+ \mu^-$ and $B_d \rightarrow \mu^+ \mu^-$ decays with the full CDF Run II data set. *Phys. Rev. D* **87**, 072003 (2013).
45. L3 Collaboration, Acciarri M. *et al.* Search for neutral B meson decays to two charged leptons. *Phys. Lett. B* **391**, 474–480 (1997).
46. DØ Collaboration, Abbott B. *et al.* Search for the decay $b \rightarrow X_s \mu^+ \mu^-$. *Phys. Lett. B* **423**, 419–426 (1998).
47. DØ Collaboration, Abazov V. *et al.* A search for the flavor-changing neutral current decay $B_s^0 \rightarrow \mu^+ \mu^-$ in $p\bar{p}$ collisions at $\sqrt{s} = 1.96$ TeV with the DØ detector. *Phys. Rev. Lett.* **94**, 071802 (2005).
48. DØ Collaboration, Abazov V. M. *et al.* Search for $B_s^0 \rightarrow \mu^+ \mu^-$ at DØ. *Phys. Rev. D* **76**, 092001 (2007).
49. DØ Collaboration, Abazov V. M. *et al.* Search for the rare decay $B_s^0 \rightarrow \mu^+ \mu^-$. *Phys. Lett. B* **693**, 539–544 (2010).
50. DØ Collaboration, Abazov V. M. *et al.* Search for the rare decay $B_s^0 \rightarrow \mu^+ \mu^-$. *Phys. Rev. D* **87**, 072006 (2013).
51. BELLE Collaboration, Chang M. *et al.* Search for $B^0 \rightarrow \ell^+ \ell^-$ at BELLE. *Phys. Rev. D* **68**, 111101 (2003).
52. BaBar Collaboration, Aubert B. *et al.* Search for decays of B^0 mesons into pairs of charged leptons: $B^0 \rightarrow e^+ e^-$, $B^0 \rightarrow \mu^+ \mu^-$, $B^0 \rightarrow e^\pm \mu^\mp$. *Phys. Rev. Lett.* **94**, 221803 (2005).
53. BaBar Collaboration, Aubert B. *et al.* Search for decays of B^0 mesons into $e^+ e^-$, $\mu^+ \mu^-$, and $e^\pm \mu^\mp$ final states. *Phys. Rev. D* **77**, 032007 (2008).
54. LHCb Collaboration, Aaij R. *et al.* Search for the rare decays $B_s^0 \rightarrow \mu^+ \mu^-$ and $B^0 \rightarrow \mu^+ \mu^-$. *Phys. Lett. B* **699**, 330–340 (2011).
55. LHCb Collaboration, Aaij R. *et al.* Strong constraints on the rare decays $B_s^0 \rightarrow \mu^+ \mu^-$ and $B^0 \rightarrow \mu^+ \mu^-$. *Phys. Rev. Lett.* **108**, 231801 (2012).
56. LHCb Collaboration, Aaij R. *et al.* Search for the rare decays $B_s^0 \rightarrow \mu^+ \mu^-$ and $B^0 \rightarrow \mu^+ \mu^-$. *Phys. Lett. B* **708**, 55–67 (2012).
57. LHCb Collaboration, Aaij R. *et al.* Measurement of the $B_s^0 \rightarrow \mu^+ \mu^-$ branching fraction and search for $B^0 \rightarrow \mu^+ \mu^-$ decays at the LHCb experiment. *Phys. Rev. Lett.* **111**, 101805 (2013).
58. CMS Collaboration, Chatrchyan S. *et al.* Search for $B_s^0 \rightarrow \mu^+ \mu^-$ and $B^0 \rightarrow \mu^+ \mu^-$ decays in pp collisions at 7 TeV. *Phys. Rev. Lett.* **107**, 191802 (2011).
59. CMS Collaboration, Chatrchyan S. *et al.* Search for $B_s^0 \rightarrow \mu^+ \mu^-$ and $B^0 \rightarrow \mu^+ \mu^-$ decays. *J. High Energy Phys.* **04**, 033 (2012).
60. ATLAS Collaboration, Aad G. *et al.* Search for the decay $B_s^0 \rightarrow \mu^+ \mu^-$ with the ATLAS detector. *Phys. Lett. B* **713**, 387–407 (2012).
61. LHCb Collaboration, Aaij R. *et al.* Updated average f_s/f_d b -hadron production fraction ratio for 7 TeV pp collisions. <http://cds.cern.ch/record/1559262> (LHCb-CONF-2013-011, 2013).
62. De Bruyn, K. *et al.* Probing new physics via the $B_s^0 \rightarrow \mu^+ \mu^-$ effective lifetime. *Phys. Rev. Lett.* **109**, 041801 (2012).
63. Khodjamirian, A., Klein, C., Mannel, T. & Wang, Y.-M. Form factors and strong couplings of heavy baryons from QCD light-cone sum rules. *J. High Energy Phys.* **09**, 106 (2011).
64. LHCb Collaboration, Aaij R. *et al.* Precision measurement of the ratio of the A_1^0 to \bar{B}^0 lifetimes. *Phys. Lett. B* **734**, 122–130 (2014).
65. ATLAS and CMS Collaborations. Procedure for the LHC Higgs boson search combination in summer 2011. <http://cds.cern.ch/record/1379837> (ATL-PHYS-PUB-2011-011, CMS NOTE 2011/005, 2011).

A. Brinkerhoff¹⁸⁷, K.M. Chan¹⁸⁷, A. Drozdetskiy¹⁸⁷, M. Hildreth¹⁸⁷, C. Jessop¹⁸⁷, D.J. Karmgard¹⁸⁷, N. Kellams¹⁸⁷, K. Lannon¹⁸⁷, S. Lynch¹⁸⁷, N. Marinelli¹⁸⁷, Y. Musienko^{187,232}, T. Pearson¹⁸⁷, M. Planer¹⁸⁷, R. Ruchti¹⁸⁷, G. Smith¹⁸⁷, N. Valls¹⁸⁷, M. Wayne¹⁸⁷, M. Wolf¹⁸⁷, A. Woodard¹⁸⁷, L. Antonelli¹⁸⁸, J. Brinson¹⁸⁸, B. Bylsma¹⁸⁸, L.S. Durkin¹⁸⁸, S. Flowers¹⁸⁸, A. Hart¹⁸⁸, C. Hill¹⁸⁸, R. Hughes¹⁸⁸, K. Kotov¹⁸⁸, T.Y. Ling¹⁸⁸, W. Luo¹⁸⁸, D. Pui¹⁸⁸, M. Rodenburg¹⁸⁸, B.L. Winer¹⁸⁸, H. Wolfe¹⁸⁸, H.W. Wulsin¹⁸⁸, O. Driga¹⁸⁹, P. Elmer¹⁸⁹, J. Hardenbrook¹⁸⁹, P. Hebeda¹⁸⁹, A. Hunt¹⁸⁹, S.A. Koay¹⁸⁹, P. Lujan¹⁸⁹, D. Marlow¹⁸⁹, T. Medvedeva¹⁸⁹, M. Mooney¹⁸⁹, J. Olsen¹⁸⁹, P. Piroué¹⁸⁹, X. Quan¹⁸⁹, H. Saka¹⁸⁹, D. Sticckland^{189,205}, C. Tully¹⁸⁹, J.S. Werner¹⁸⁹, A. Zuranski¹⁸⁹, E. Brownson¹⁹⁰, S. Malik¹⁹⁰, H. Mendez¹⁹⁰, J.E. Ramirez Vargas¹⁹⁰, V.E. Barnes¹⁹¹, D. Benedetti¹⁹¹, D. Bortoletto¹⁹¹, M. De Mattia¹⁹¹, L. Gutay¹⁹¹, Z. Hu¹⁹¹, M.K. Jha¹⁹¹, M. Jones¹⁹¹, K. Jung¹⁹¹, M. Kress¹⁹¹, N. Leonardo¹⁹¹, D.H. Miller¹⁹¹, N. Neumeister¹⁹¹, B.C. Radburn-Smith¹⁹¹, X. Shi¹⁹¹, I. Shipsey¹⁹¹, D. Silvers¹⁹¹, A. Svyatkovskiy¹⁹¹, F. Wang¹⁹¹, W. Xie¹⁹¹, L. Xu¹⁹¹, J. Zablocki¹⁹¹, N. Parashar¹⁹², J. Stupak¹⁹², A. Adair¹⁹³, B. Akgun¹⁹³, K.M. Ecklund¹⁹³, F.J.M. Geurts¹⁹³, W. Li¹⁹³, B. Michlin¹⁹³, B.P. Padley¹⁹³, R. Redjimi¹⁹³, J. Roberts¹⁹³, J. Zabel¹⁹³, B. Betchart¹⁹⁴, A. Bodek¹⁹⁴, R. Covarelli¹⁹⁴, P. de Barbaro¹⁹⁴, R. Demina¹⁹⁴, Y. Eshaq¹⁹⁴, T. Ferbel¹⁹⁴, A. Garcia-Bellido¹⁹⁴, P. Goldenfisz¹⁹⁴, J. Han¹⁹⁴, A. Harel¹⁹⁴, A. Khukhunaishvili¹⁹⁴, S. Korjanevski¹⁹⁴, G. Petrillo¹⁹⁴, D. Vishnevskiy¹⁹⁴, R. Ciesielski¹⁹⁵, L. Demortier¹⁹⁵, K. Goulianos¹⁹⁵, C. Mesropian¹⁹⁵, S. Arora¹⁹⁶, A. Barker¹⁹⁶, J.P. Chou¹⁹⁶, C. Contreras-Campana¹⁹⁶, E. Contreras-Campana¹⁹⁶, D. Duggan¹⁹⁶, D. Ferencek¹⁹⁶, Y. Gershtein¹⁹⁶, R. Gray¹⁹⁶, E. Halkiadakis¹⁹⁶, D. Hidas¹⁹⁶, S. Kaplan¹⁹⁶, A. Lath¹⁹⁶, S. Panwalkar¹⁹⁶, M. Park¹⁹⁶, R. Patel¹⁹⁶, S. Salur¹⁹⁶, S. Schnetzer¹⁹⁶, S. Somalwar¹⁹⁶, R. Stone¹⁹⁶, S. Thomas¹⁹⁶, P. Thomassen¹⁹⁶, M. Walker¹⁹⁶, K. Rose¹⁹⁷, S. Spanier¹⁹⁷, A. York¹⁹⁷, O. Bouhali^{198,258}, A. Castaneda Hernandez¹⁹⁸, R. Eusebi¹⁹⁸, W. Flanagan¹⁹⁸, J. Gilmore¹⁹⁸, T. Kamon^{198,259}, V. Khokhlovich¹⁹⁸, V. Krutlyov¹⁹⁸, R. Montalvo¹⁹⁸, I. Osipenko¹⁹⁸, Y. Pakhotin¹⁹⁸, A. Perloff¹⁹⁸, J. Roe¹⁹⁸, A. Rose¹⁹⁸, A. Safonov¹⁹⁸, I. Suarez¹⁹⁸, A. Tatarinov¹⁹⁸, K.M. Umer¹⁹⁸, N. Akchurin¹⁹⁹, C. Cowden¹⁹⁹, J. Damgov¹⁹⁹, C. Dragou¹⁹⁹, P.R. Duder¹⁹⁹, J. Faulkner¹⁹⁹, K. Kovitanggoon¹⁹⁹, S. Kunori¹⁹⁹, S.W. Lee¹⁹⁹, T. Libeiro¹⁹⁹, I. Volobouev¹⁹⁹, E. Appelt²⁰⁰, A.G. Delannoy²⁰⁰, S. Greene²⁰⁰, A. Gurrola²⁰⁰, W. Johns²⁰⁰, C. Maguire²⁰⁰, Y. Mao²⁰⁰, A. Melo²⁰⁰, M. Sharma²⁰⁰, P. Sheldon²⁰⁰, B. Snook²⁰⁰, S. Tuo²⁰⁰, J. Velkovska²⁰⁰, M.W. Arenton²⁰¹, S. Boutle²⁰¹, B. Cox²⁰¹, B. Francis²⁰¹, J. Goodell²⁰¹, R. Hirosky²⁰¹, A. Ledovsky²⁰¹, H. Li²⁰¹, C. Lin²⁰¹, C. Ne²⁰¹, J. Wood²⁰¹, C. Clarke²⁰², R. Harr²⁰², P.E. Karchin²⁰², C. Kottachchi Kankanamge Don²⁰², P. Lamichhane²⁰², J. Sturdy²⁰², D.A. Belknap²⁰³, D. Carlsmith²⁰³, M. Cepeda²⁰³, S. Dasu²⁰³, L. Dodd²⁰³, S. Duric²⁰³, E. Friis²⁰³, R. Hall-Wilton²⁰³, M. Herndon²⁰³, A. Hervé²⁰³, P. Klabbers²⁰³, A. Lanaro²⁰³, C. Lazaridis²⁰³, A. Levine²⁰³, R. Loveless²⁰³, A. Mohapatra²⁰³, I. Ojalvo²⁰³, T. Perry²⁰³, G.A. Pierro²⁰³, G. Polese²⁰³, I. Ross²⁰³, T. Sarangi²⁰³, A. Savin²⁰³, W.H. Smith²⁰³, D. Taylor²⁰³, C. Vuosalo²⁰³ & N. Woods²⁰³

Primary affiliations

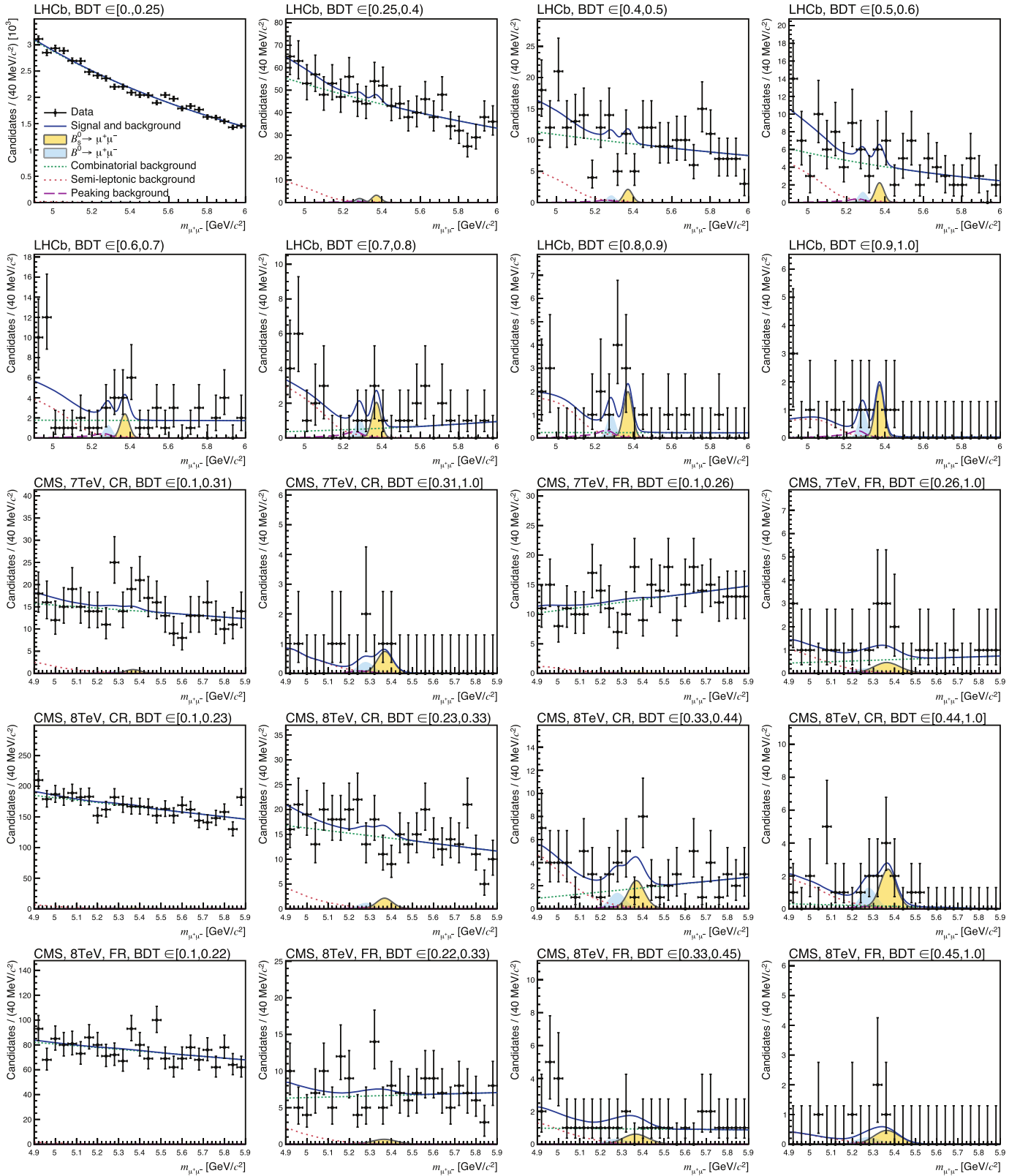
¹Yerevan Physics Institute, Yerevan, Armenia. ²Institut für Hochenergiephysik der OeAW, Wien, Austria. ³National Centre for Particle and High Energy Physics, Minsk, Belarus. ⁴Universiteit Antwerpen, Antwerpen, Belgium. ⁵Vrije Universiteit Brussel, Brussel, Belgium. ⁶Université Libre de Bruxelles, Bruxelles, Belgium. ⁷Ghent University, Ghent, Belgium. ⁸Université Catholique de Louvain, Louvain-la-Neuve, Belgium. ⁹Université de Mons, Mons, Belgium. ¹⁰Centro Brasileiro de Pesquisas Físicas, Rio de Janeiro, Brazil. ¹¹Universidade do Estado do Rio de Janeiro, Rio de Janeiro, Brazil. ¹²Universidade Estadual Paulista, Universidade Federal do ABC, São Paulo, Brazil. ¹³Universidade Estadual Paulista. ¹⁴Universidade Federal do ABC. ¹⁵Institute for Nuclear Research and Nuclear Energy, Sofia, Bulgaria. ¹⁶University of Sofia, Sofia, Bulgaria. ¹⁷Institute of High Energy Physics, Beijing, China. ¹⁸State Key Laboratory of Nuclear Physics and Technology, Peking University, Beijing, China. ¹⁹Universidad de Los Andes, Bogotá, Colombia. ²⁰University of Split, Faculty of Electrical Engineering, Mechanical Engineering and Naval Architecture, Split, Croatia. ²¹University of Split, Faculty of Science, Split, Croatia. ²²Institute Rudjer Boskovic, Zagreb, Croatia. ²³University of Cyprus, Nicosia, Cyprus. ²⁴Charles University, Prague, Czech Republic. ²⁵Academy of Scientific Research and Technology of the Arab Republic of Egypt, Egyptian Network of High Energy Physics, Cairo, Egypt. ²⁶National Institute of Chemical Physics and Biophysics, Tallinn, Estonia. ²⁷Department of Physics, University of Helsinki, Helsinki, Finland. ²⁸Helsinki Institute of Physics, Helsinki, Finland. ²⁹Lappeenranta University of Technology, Lappeenranta, Finland. ³⁰DSM/IRFU, CEA/Saclay, Gif-sur-Yvette, France. ³¹Laboratoire Leprince-Ringuet, Ecole Polytechnique, IN2P3-CNRS, Palaiseau, France. ³²Institut Pluridisciplinaire Hubert Curien, Université de Strasbourg, Université de Haute Alsace Mulhouse, CNRS/IN2P3, Strasbourg, France. ³³Centre de Calcul de l'Institut National de Physique Nucléaire et de Physique des Particules, CNRS/IN2P3, Villeurbanne, France. ³⁴Université de Lyon, Université Claude Bernard Lyon 1, CNRS-IN2P3, Institut de Physique Nucléaire de Lyon, Villeurbanne, France. ³⁵Institute of High Energy Physics and Informatization, Tbilisi State University, Tbilisi, Georgia. ³⁶RWTH Aachen University, I. Physikalisches Institut, Aachen, Germany. ³⁷RWTH Aachen University, III. Physikalisches Institut A, Aachen, Germany. ³⁸RWTH Aachen University, III. Physikalisches Institut B, Aachen, Germany. ³⁹Deutsches Elektronen-Synchrotron, Hamburg, Germany. ⁴⁰University of Hamburg, Hamburg, Germany. ⁴¹Institut für Experimentelle Kernphysik, Karlsruhe, Germany. ⁴²Institute of Nuclear and Particle Physics (INPP), NCSR Demokritos, Aghia Paraskevi, Greece. ⁴³University of Athens, Athens, Greece. ⁴⁴University of Ioánnina, Ioánnina, Greece. ⁴⁵Wigner Research Centre for Physics, Budapest, Hungary. ⁴⁶Institute of Nuclear Research ATOMKI, Debrecen, Hungary. ⁴⁷University of Debrecen, Debrecen, Hungary. ⁴⁸National Institute of Science Education and Research, Bhubaneswar, India. ⁴⁹Panjab University, Chandigarh, India. ⁵⁰University of Delhi, Delhi, India. ⁵¹Saha Institute of Nuclear Physics, Kolkata, India. ⁵²Bhabha Atomic Research Centre, Mumbai, India. ⁵³Tata Institute of Fundamental Research, Mumbai, India. ⁵⁴Institute for Research in Fundamental Sciences (IPM), Tehran, Iran. ⁵⁵University College Dublin, Dublin, Ireland. ⁵⁶INFN Sezione di Bari, Università di Bari, Politecnico di Bari, Bari, Italy. ⁵⁷INFN Sezione di Bari. ⁵⁸Università di Bari. ⁵⁹Politecnico di Bari. ⁶⁰INFN Sezione di Bologna, Università

di Bologna, Bologna, Italy. ⁶¹INFN Sezione di Bologna. ⁶²Università di Bologna. ⁶³INFN Sezione di Catania, Università di Catania, CSFNSM, Catania, Italy. ⁶⁴INFN Sezione di Catania. ⁶⁵Università di Catania. ⁶⁶CSFNSM. ⁶⁷INFN Sezione di Firenze, Università di Firenze, Firenze, Italy. ⁶⁸INFN Sezione di Firenze. ⁶⁹Università di Firenze. ⁷⁰INFN Laboratori Nazionali di Frascati, Frascati, Italy. ⁷¹INFN Sezione di Genova, Università di Genova, Genova, Italy. ⁷²INFN Sezione di Genova. ⁷³Università di Genova. ⁷⁴INFN Sezione di Milano-Bicocca, Università di Milano-Bicocca, Milano, Italy. ⁷⁵INFN Sezione di Milano-Bicocca. ⁷⁶Università di Milano-Bicocca. ⁷⁷INFN Sezione di Napoli, Università di Napoli 'Federico II', Università della Basilicata (Potenza), Università G. Marconi (Roma), Napoli, Italy. ⁷⁸INFN Sezione di Napoli. ⁷⁹Università di Napoli 'Federico II'. ⁸⁰Università della Basilicata (Potenza). ⁸¹Università G. Marconi (Roma). ⁸²INFN Sezione di Padova, Università di Padova, Università di Trento (Trento), Padova, Italy. ⁸³INFN Sezione di Padova. ⁸⁴Università di Padova. ⁸⁵Università di Trento (Trento). ⁸⁶INFN Sezione di Pavia, Università di Pavia, Pavia, Italy. ⁸⁷INFN Sezione di Pavia. ⁸⁸Università di Pavia. ⁸⁹INFN Sezione di Perugia, Università di Perugia, Perugia, Italy. ⁹⁰INFN Sezione di Perugia. ⁹¹Università di Perugia. ⁹²INFN Sezione di Pisa, Università di Pisa, Scuola Normale Superiore di Pisa, Pisa, Italy. ⁹³INFN Sezione di Pisa. ⁹⁴Università di Pisa. ⁹⁵Scuola Normale Superiore di Pisa. ⁹⁶INFN Sezione di Roma, Università di Roma, Roma, Italy. ⁹⁷INFN Sezione di Roma. ⁹⁸Università di Roma. ⁹⁹INFN Sezione di Torino, Università di Torino, Università del Piemonte Orientale (Novara), Torino, Italy. ¹⁰⁰INFN Sezione di Torino. ¹⁰¹Università di Torino. ¹⁰²Università del Piemonte Orientale (Novara). ¹⁰³INFN Sezione di Trieste, Università di Trieste, Trieste, Italy. ¹⁰⁴INFN Sezione di Trieste. ¹⁰⁵Università di Trieste. ¹⁰⁶Kangwon National University, Chunchon, Korea. ¹⁰⁷Kyungpook National University, Daegu, Korea. ¹⁰⁸Chonbuk National University, Jeonju, Korea. ¹⁰⁹Chonnam National University, Institute for Universe and Elementary Particles, Kwangju, Korea. ¹¹⁰Korea University, Seoul, Korea. ¹¹¹Seoul National University, Seoul, Korea. ¹¹²University of Seoul, Seoul, Korea. ¹¹³Sungkyunkwan University, Suwon, Korea. ¹¹⁴Vilnius University, Vilnius, Lithuania. ¹¹⁵National Centre for Particle Physics, Universiti Malaysia, Kuala Lumpur, Malaysia. ¹¹⁶Centro de Investigación y de Estudios Avanzados del IPN, Mexico City, Mexico. ¹¹⁷Universidad Iberoamericana, Mexico City, Mexico. ¹¹⁸Benemerita Universidad Autónoma de Puebla, Puebla, Mexico. ¹¹⁹Universidad Autónoma de San Luis Potosí, San Luis Potosí, Mexico. ¹²⁰University of Auckland, Auckland, New Zealand. ¹²¹University of Canterbury, Christchurch, New Zealand. ¹²²National Centre for Physics, Quaid-I-Azam University, Islamabad, Pakistan. ¹²³National Centre for Nuclear Research, Swierk, Poland. ¹²⁴Institute of Experimental Physics, Faculty of Physics, University of Warsaw, Warsaw, Poland. ¹²⁵Laboratório de Instrumentação e Física Experimental de Partículas, Lisboa, Portugal. ¹²⁶Joint Institute for Nuclear Research, Dubna, Russia. ¹²⁷Petersburg Nuclear Physics Institute, Gatchina (St. Petersburg), Russia. ¹²⁸Institute for Nuclear Research, Moscow, Russia. ¹²⁹Institute for Theoretical and Experimental Physics, Moscow, Russia. ¹³⁰P.N. Lebedev Physical Institute, Moscow, Russia. ¹³¹Skobeltsyn Institute of Nuclear Physics, Lomonosov Moscow State University, Moscow, Russia. ¹³²State Research Center of Russian Federation, Institute for High Energy Physics, Protvino, Russia. ¹³³University of Belgrade, Faculty of Physics and Vinca Institute of Nuclear Sciences, Belgrade, Serbia. ¹³⁴Centro de Investigaciones Energéticas Medioambientales y Tecnológicas (CIEMAT), Madrid, Spain. ¹³⁵Universidad Autónoma de Madrid, Madrid, Spain. ¹³⁶Universidad de Oviedo, Oviedo, Spain. ¹³⁷Instituto de Física de Cantabria (IFCA), CSIC-Universidad de Cantabria, Santander, Spain. ¹³⁸CERN, European Organization for Nuclear Research, Geneva, Switzerland. ¹³⁹Paul Scherrer Institut, Villigen, Switzerland. ¹⁴⁰Institute for Particle Physics, ETH Zurich, Zurich, Switzerland. ¹⁴¹Universität Zürich, Zurich, Switzerland. ¹⁴²National Central University, Chung-Li, Taiwan. ¹⁴³National Taiwan University (NTU), Taipei, Taiwan. ¹⁴⁴Chulalongkorn University, Faculty of Science, Department of Physics, Bangkok, Thailand. ¹⁴⁵Cukurova University, Adana, Turkey. ¹⁴⁶Middle East Technical University, Physics Department, Ankara, Turkey. ¹⁴⁷Bogaziçi University, Istanbul, Turkey. ¹⁴⁸Istanbul Technical University, Istanbul, Turkey. ¹⁴⁹National Scientific Center, Kharkov Institute of Physics and Technology, Kharkov, Ukraine. ¹⁵⁰University of Bristol, Bristol, United Kingdom. ¹⁵¹Rutherford Appleton Laboratory, Didcot, United Kingdom. ¹⁵²Imperial College, London, United Kingdom. ¹⁵³Brunel University, Uxbridge, United Kingdom. ¹⁵⁴Baylor University, Waco, USA. ¹⁵⁵The University of Alabama, Tuscaloosa, USA. ¹⁵⁶Boston University, Boston, USA. ¹⁵⁷Brown University, Providence, USA. ¹⁵⁸University of California, Davis, Davis, USA. ¹⁵⁹University of California, Los Angeles, USA. ¹⁶⁰University of California, Riverside, Riverside, USA. ¹⁶¹University of California, San Diego, La Jolla, USA. ¹⁶²University of California, Santa Barbara, Santa Barbara, USA. ¹⁶³California Institute of Technology, Pasadena, USA. ¹⁶⁴Carnegie Mellon University, Pittsburgh, USA. ¹⁶⁵University of Colorado at Boulder, Boulder, USA. ¹⁶⁶Cornell University, Ithaca, USA. ¹⁶⁷Fairfield University, Fairfield, USA. ¹⁶⁸Fermi National Accelerator Laboratory, Batavia, USA. ¹⁶⁹University of Florida, Gainesville, USA. ¹⁷⁰Florida International University, Miami, USA. ¹⁷¹Florida State University, Tallahassee, USA. ¹⁷²Florida Institute of Technology, Melbourne, USA. ¹⁷³University of Illinois at Chicago (UIC), Chicago, USA. ¹⁷⁴The University of Iowa, Iowa City, USA. ¹⁷⁵Johns Hopkins University, Baltimore, USA. ¹⁷⁶The University of Kansas, Lawrence, USA. ¹⁷⁷Kansas State University, Manhattan, USA. ¹⁷⁸Lawrence Livermore National Laboratory, Livermore, USA. ¹⁷⁹University of Maryland, College Park, USA. ¹⁸⁰Massachusetts Institute of Technology, Cambridge, USA. ¹⁸¹University of Minnesota, Minneapolis, USA. ¹⁸²University of Mississippi, Oxford, USA. ¹⁸³University of Nebraska-Lincoln, Lincoln, USA. ¹⁸⁴State University of New York at Buffalo, Buffalo, USA. ¹⁸⁵Northeastern University, Boston, USA. ¹⁸⁶Northwestern University, Evanston, USA. ¹⁸⁷University of Notre Dame, Notre Dame, USA. ¹⁸⁸The Ohio State University, Columbus, USA. ¹⁸⁹Princeton University, Princeton, USA. ¹⁹⁰University of Puerto Rico, Mayaguez, USA. ¹⁹¹Purdue University, West Lafayette, USA. ¹⁹²Purdue University Calumet, Hammond, USA. ¹⁹³Rice University, Houston, USA. ¹⁹⁴University of Rochester, Rochester, USA. ¹⁹⁵The Rockefeller University, New York, USA. ¹⁹⁶Rutgers, The State University of New Jersey, Piscataway, USA. ¹⁹⁷University of Tennessee, Knoxville, USA. ¹⁹⁸Texas A&M University, College Station, USA. ¹⁹⁹Texas Tech University, Lubbock, USA. ²⁰⁰Vanderbilt University, Nashville, USA. ²⁰¹University of Virginia, Charlottesville, USA. ²⁰²Wayne State University, Detroit, USA. ²⁰³University of Wisconsin, Madison, USA.

France.⁷LAL, Université Paris-Sud, CNRS/IN2P3, Orsay, France.⁸LPNHE, Université Pierre et Marie Curie, Université Paris Diderot, CNRS/IN2P3, Paris, France.⁹Fakultät Physik, Technische Universität Dortmund, Dortmund, Germany.¹⁰Max-Planck-Institut für Kernphysik (MPIK), Heidelberg, Germany.¹¹Physikalisches Institut, Ruprecht-Karls-Universität Heidelberg, Heidelberg, Germany.¹²School of Physics, University College Dublin, Dublin, Ireland.¹³Sezione INFN di Bari, Bari, Italy.¹⁴Sezione INFN di Bologna, Bologna, Italy.¹⁵Sezione INFN di Cagliari, Cagliari, Italy.¹⁶Sezione INFN di Ferrara, Ferrara, Italy.¹⁷Sezione INFN di Firenze, Firenze, Italy.¹⁸Laboratori Nazionali dell'INFN di Frascati, Frascati, Italy.¹⁹Sezione INFN di Genova, Genova, Italy.²⁰Sezione INFN di Milano Bicocca, Milano, Italy.²¹Sezione INFN di Milano, Milano, Italy.²²Sezione INFN di Padova, Padova, Italy.²³Sezione INFN di Pisa, Pisa, Italy.²⁴Sezione INFN di Roma Tor Vergata, Roma, Italy.²⁵Sezione INFN di Roma La Sapienza, Roma, Italy.²⁶Henryk Niewodniczanski Institute of Nuclear Physics Polish Academy of Sciences, Kraków, Poland.²⁷AGH - University of Science and Technology, Faculty of Physics and Applied Computer Science, Kraków, Poland.²⁸National Center for Nuclear Research (NCBJ), Warsaw, Poland.²⁹Horia Hulubei National Institute of Physics and Nuclear Engineering, Bucharest-Magurele, Romania.³⁰Petersburg Nuclear Physics Institute (PNPI), Gatchina, Russia.³¹Institute of Theoretical and Experimental Physics (ITEP), Moscow, Russia.³²Institute of Nuclear Physics, Moscow State University (SINP MSU), Moscow, Russia.³³Institute for Nuclear Research of the Russian Academy of Sciences (INR RAN), Moscow, Russia.³⁴Budker Institute of Nuclear Physics (SB RAS) and Novosibirsk State University, Novosibirsk, Russia.³⁵Institute for High Energy Physics (IHEP), Protvino, Russia.³⁶Universitat de Barcelona, Barcelona, Spain.³⁷Universidad de Santiago de Compostela, Santiago de Compostela, Spain.³⁸European Organization for Nuclear Research (CERN), Geneva, Switzerland.³⁹Ecole Polytechnique Fédérale de Lausanne (EPFL), Lausanne, Switzerland.⁴⁰Physik-Institut, Universität Zürich, Zürich, Switzerland.⁴¹Nikhef National Institute for Subatomic Physics, Amsterdam, The Netherlands.⁴²Nikhef National Institute for Subatomic Physics and VU University Amsterdam, Amsterdam, The Netherlands.⁴³NSC Kharkiv Institute of Physics and Technology (NSC KIPT), Kharkiv, Ukraine.⁴⁴Institute for Nuclear Research of the National Academy of Sciences (KINR), Kyiv, Ukraine.⁴⁵University of Birmingham, Birmingham, United Kingdom.⁴⁶H.H. Wills Physics Laboratory, University of Bristol, Bristol, United Kingdom.⁴⁷Cavendish Laboratory, University of Cambridge, Cambridge, United Kingdom.⁴⁸Department of Physics, University of Warwick, Coventry, United Kingdom.⁴⁹STFC Rutherford Appleton Laboratory, Didcot, United Kingdom.⁵⁰School of Physics and Astronomy, University of Edinburgh, Edinburgh, United Kingdom.⁵¹School of Physics and Astronomy, University of Glasgow, Glasgow, United Kingdom.⁵²Oliver Lodge Laboratory, University of Liverpool, Liverpool, United Kingdom.⁵³Imperial College London, London, United Kingdom.⁵⁴School of Physics and Astronomy, University of Manchester, Manchester, United Kingdom.⁵⁵Department of Physics, University of Oxford, Oxford, United Kingdom.⁵⁶Massachusetts Institute of Technology, Cambridge, MA, United States.⁵⁷University of Cincinnati, Cincinnati, OH, United States.⁵⁸University of Maryland, College Park, MD, United States.⁵⁹Syracuse University, Syracuse, NY, United States.⁶⁰Pontificia Universidade Católica do Rio de Janeiro (PUC-Rio), Rio de Janeiro, Brazil; Universidade Federal do Rio de Janeiro (UFRJ), Rio de Janeiro, Brazil.⁶¹Institute of Particle Physics, Central China Normal University, Wuhan, Hubei, China; Center for High Energy Physics, Tsinghua University, Beijing, China.⁶²Departamento de Física, Universidad Nacional de Colombia, Bogotá, Colombia; LPNHE, Université Pierre et Marie Curie, Université Paris Diderot, CNRS/IN2P3, Paris, France.⁶³Institut für Physik, Universität Rostock, Rostock, Germany; Physikalisches Institut, Ruprecht-Karls-Universität Heidelberg, Heidelberg, Germany.⁶⁴National Research Centre Kurchatov Institute, Moscow, Russia; Institute of Theoretical and Experimental Physics (ITEP), Moscow, Russia.⁶⁵Instituto de Física Corpuscular (IFIC), Universitat de Valencia-CSIC, Valencia, Spain; Universitat de Barcelona, Barcelona, Spain.⁶⁶Van Swinderen Institute, University of Groningen, Groningen, The Netherlands; Nikhef National Institute for Subatomic Physics, Amsterdam, The Netherlands.⁶⁷Celal Bayar University, Manisa, Turkey; European Organization for Nuclear Research (CERN), Geneva, Switzerland.

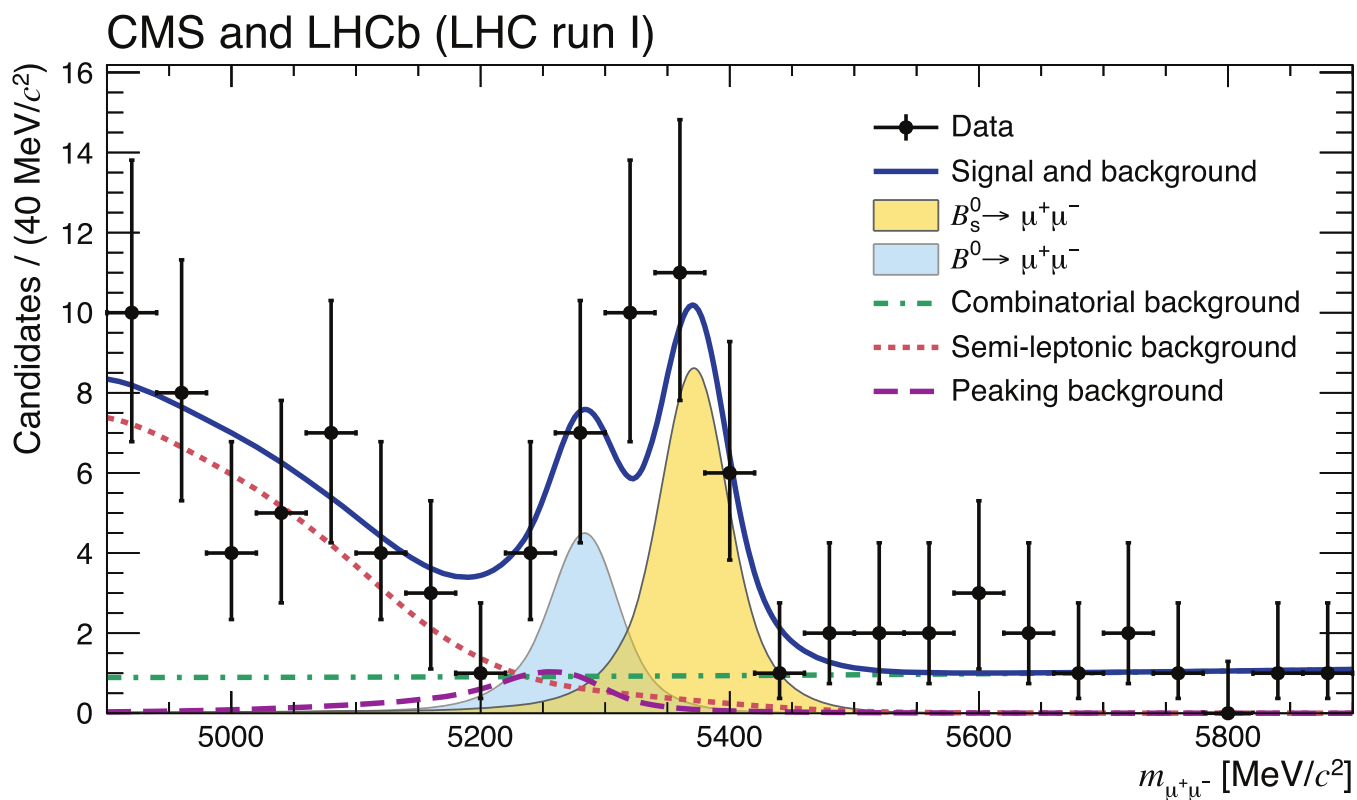
Secondary affiliations

⁶⁸Università di Firenze, Firenze, Italy.⁶⁹Università di Ferrara, Ferrara, Italy.⁷⁰Università della Basilicata, Potenza, Italy.⁷¹Università di Modena e Reggio Emilia, Modena, Italy.⁷²Università di Milano Bicocca, Milano, Italy.⁷³LIFAELS, La Salle, Universitat Ramon Llull, Barcelona, Spain.⁷⁴Università di Bologna, Bologna, Italy.⁷⁵Università di Roma Tor Vergata, Roma, Italy.⁷⁶Università di Genova, Genova, Italy.⁷⁷Scuola Normale Superiore, Pisa, Italy.⁷⁸Politecnico di Milano, Milano, Italy.⁷⁹Universidade Federal do Triângulo Mineiro (UFMT), Uberaba-MG, Brazil.⁸⁰AGH - University of Science and Technology, Faculty of Computer Science, Electronics and Telecommunications, Kraków, Poland.⁸¹Università di Padova, Padova, Italy.⁸²Università di Cagliari, Cagliari, Italy.⁸³Hanoi University of Science, Hanoi, Viet Nam.⁸⁴Università di Bari, Bari, Italy.⁸⁵Università degli Studi di Milano, Milano, Italy.⁸⁶Università di Roma La Sapienza, Roma, Italy.⁸⁷Università di Pisa, Pisa, Italy.⁸⁸Università di Urbino, Urbino, Italy.⁸⁹P.N. Lebedev Physical Institute, Russian Academy of Science (LPI RAS), Moscow, Russia.



Extended Data Figure 1 | Distribution of the dimuon invariant mass $m_{\mu^+\mu^-}$ in each of the 20 categories. Superimposed on the data points in black are the combined fit (solid blue) and its components: the B_s^0 (yellow shaded) and B^0 (light-blue shaded) signal components; the combinatorial background (dashed-dotted green); the sum of the semi-leptonic backgrounds (dotted salmon); and the peaking backgrounds (dashed violet). The categories are defined by the

range of BDT values for LHCb, and for CMS, by centre-of-mass energy, by the region of the detector in which the muons are detected, and by the range of BDT values. Categories for which both muons are detected in the central region of the CMS detector are denoted with CR, those for which at least one muon was detected into the forward region with FR.



Extended Data Figure 2 | Distribution of the dimuon invariant mass $m_{\mu^+\mu^-}$ for the best six categories. Categories are ranked according to values of $S/(S+B)$ where S and B are the numbers of signal events expected assuming the SM rates and background events under the B_s^0 peak for a given category, respectively. The mass distribution for the six highest-ranking categories, three

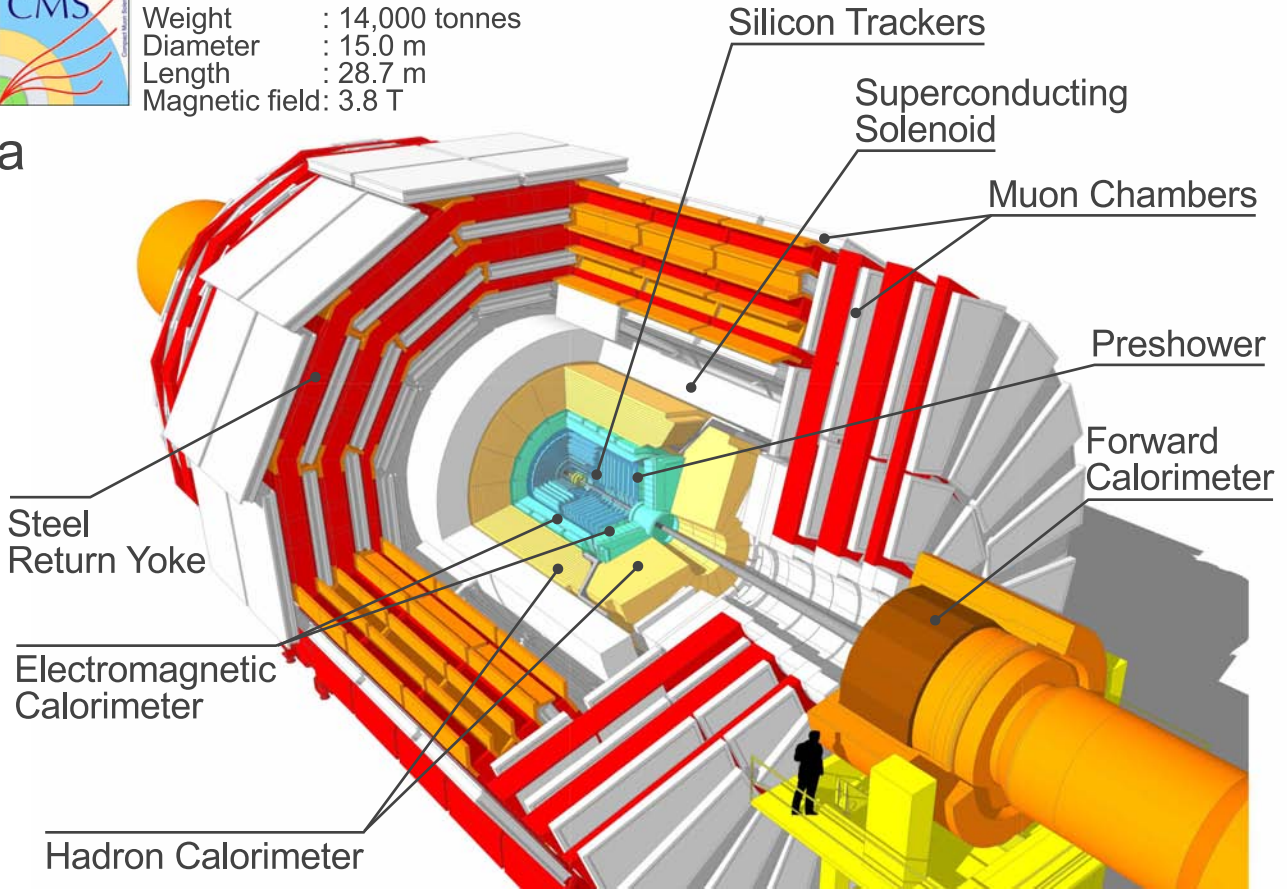
per experiment, is shown. Superimposed on the data points in black are the combined full fit (solid blue) and its components: the B_s^0 (yellow shaded) and B^0 (light-blue shaded) signal components; the combinatorial background (dash-dotted green); the sum of the semi-leptonic backgrounds (dotted salmon); and the peaking backgrounds (dashed violet).



CMS Detector

Weight : 14,000 tonnes
 Diameter : 15.0 m
 Length : 28.7 m
 Magnetic field: 3.8 T

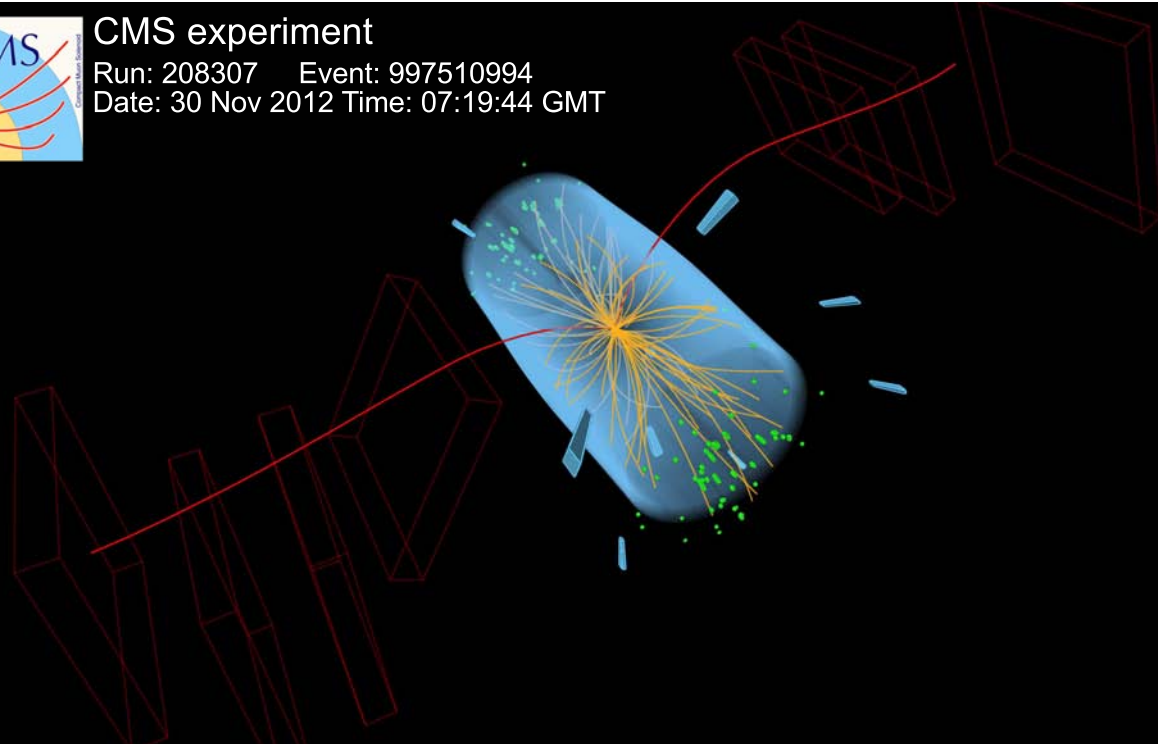
a



CMS experiment

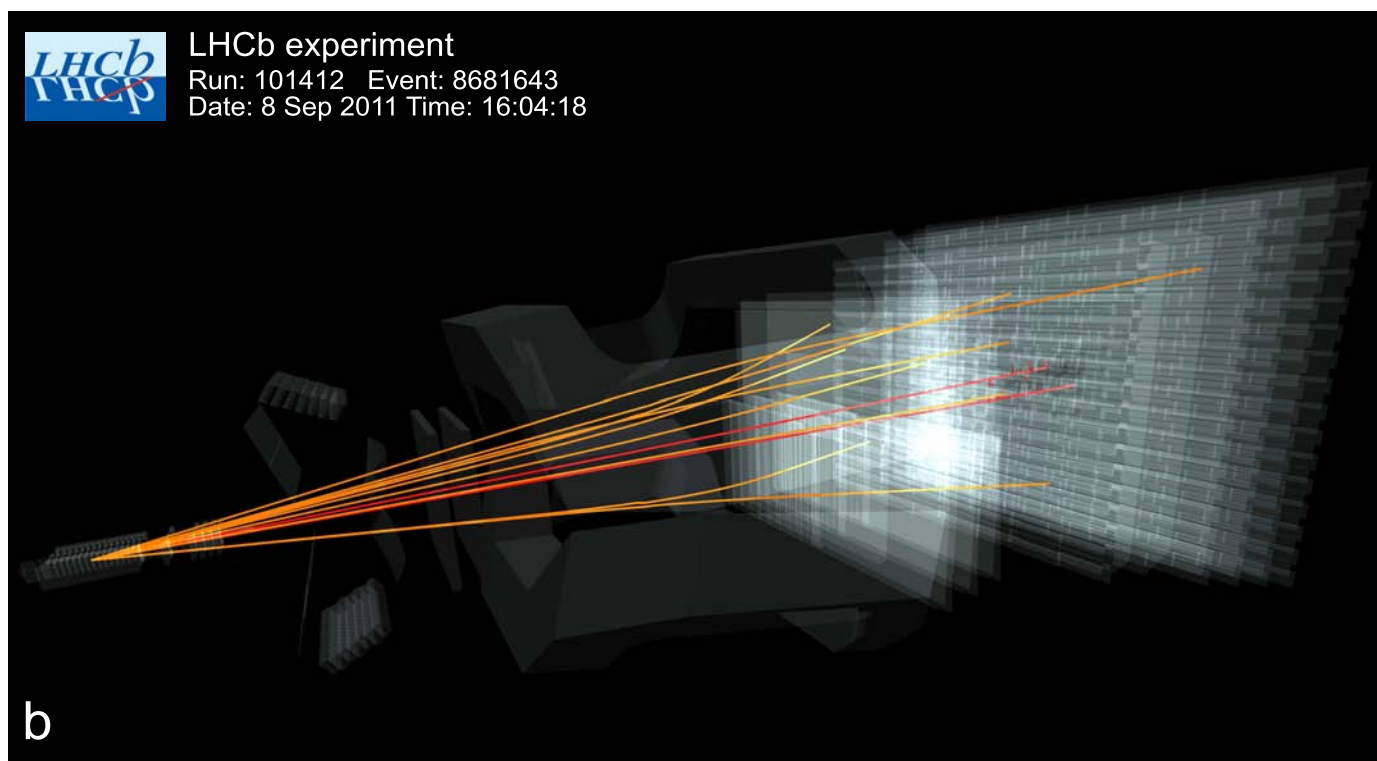
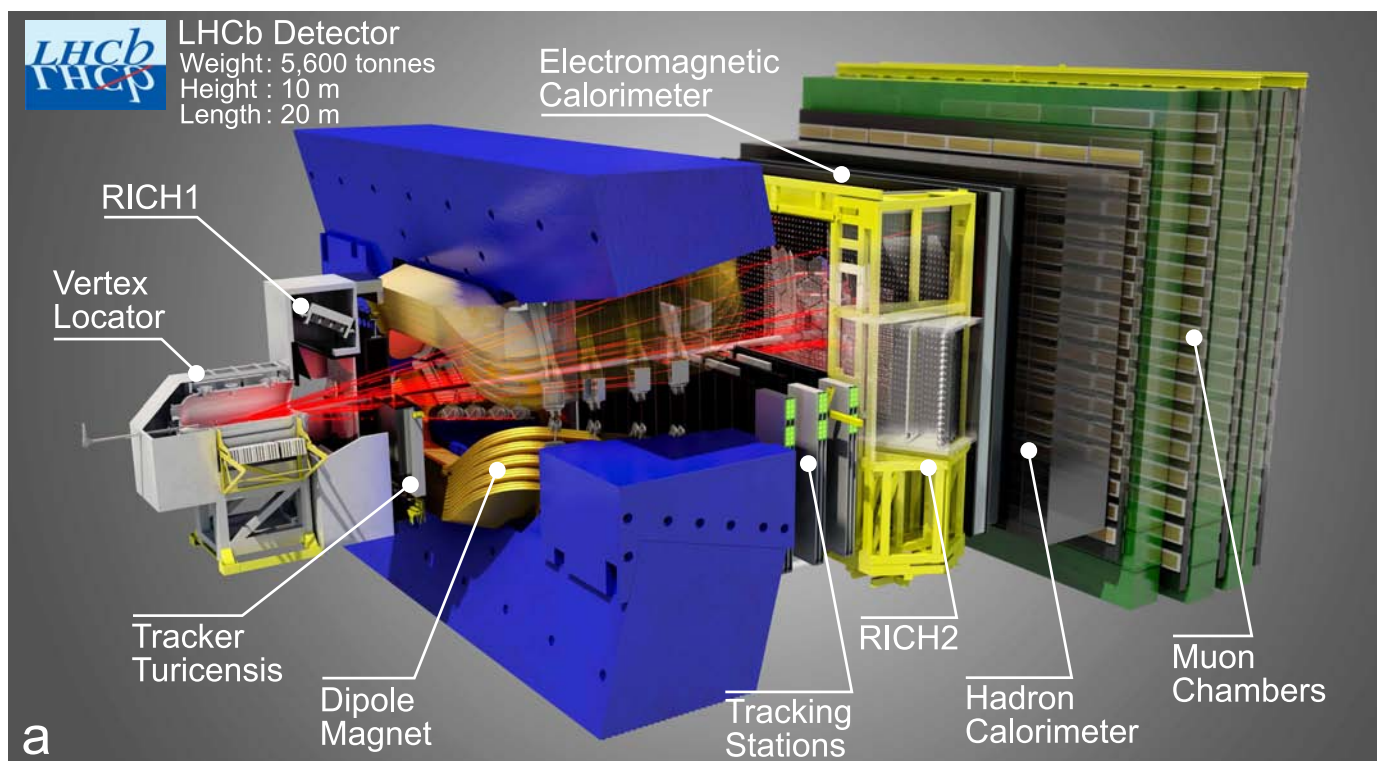
Run: 208307 Event: 997510994
 Date: 30 Nov 2012 Time: 07:19:44 GMT

b



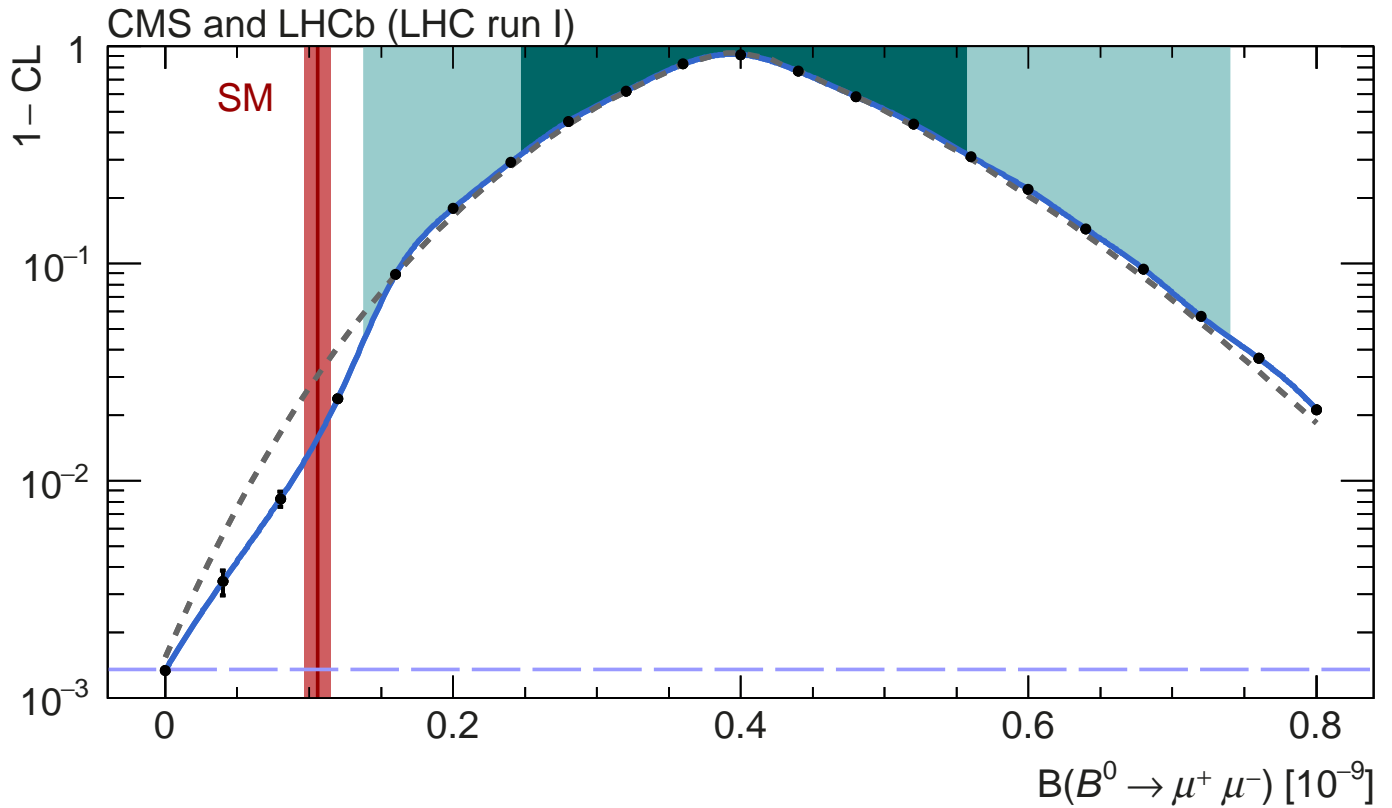
Extended Data Figure 3 | Schematic of the CMS detector and event display for a candidate $B_s^0 \rightarrow \mu^+ \mu^-$ decay at CMS. a, The CMS detector and its components; see ref. 20 for details. b, A candidate $B_s^0 \rightarrow \mu^+ \mu^-$ decay produced

in proton–proton collisions at 8 TeV in 2012 and recorded in the CMS detector. The red arched curves represent the trajectories of the muons from the B_s^0 decay candidate.



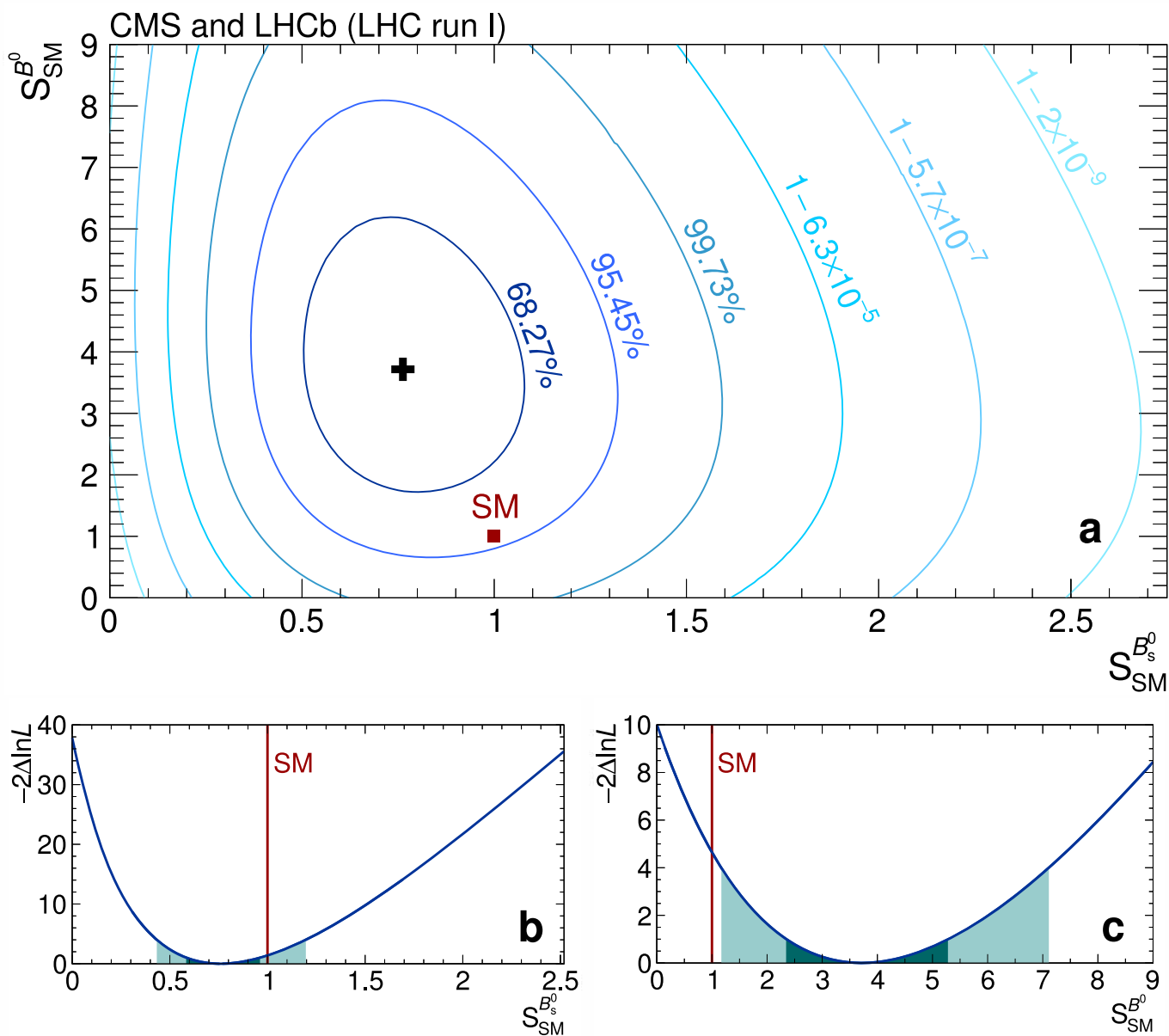
Extended Data Figure 4 | Schematic of the LHCb detector and event display for a candidate $B_s^0 \rightarrow \mu^+ \mu^-$ decay at LHCb. **a**, The LHCb detector and its components; see ref. 21 for details. **b**, A candidate $B_s^0 \rightarrow \mu^+ \mu^-$ decay produced in proton–proton collisions at 7 TeV in 2011 and recorded in the LHCb

detector. The proton–proton collision occurs on the left-hand side, at the origin of the trajectories depicted with the orange curves. The red curves represent the trajectories of the muons from the B_s^0 candidate decay.



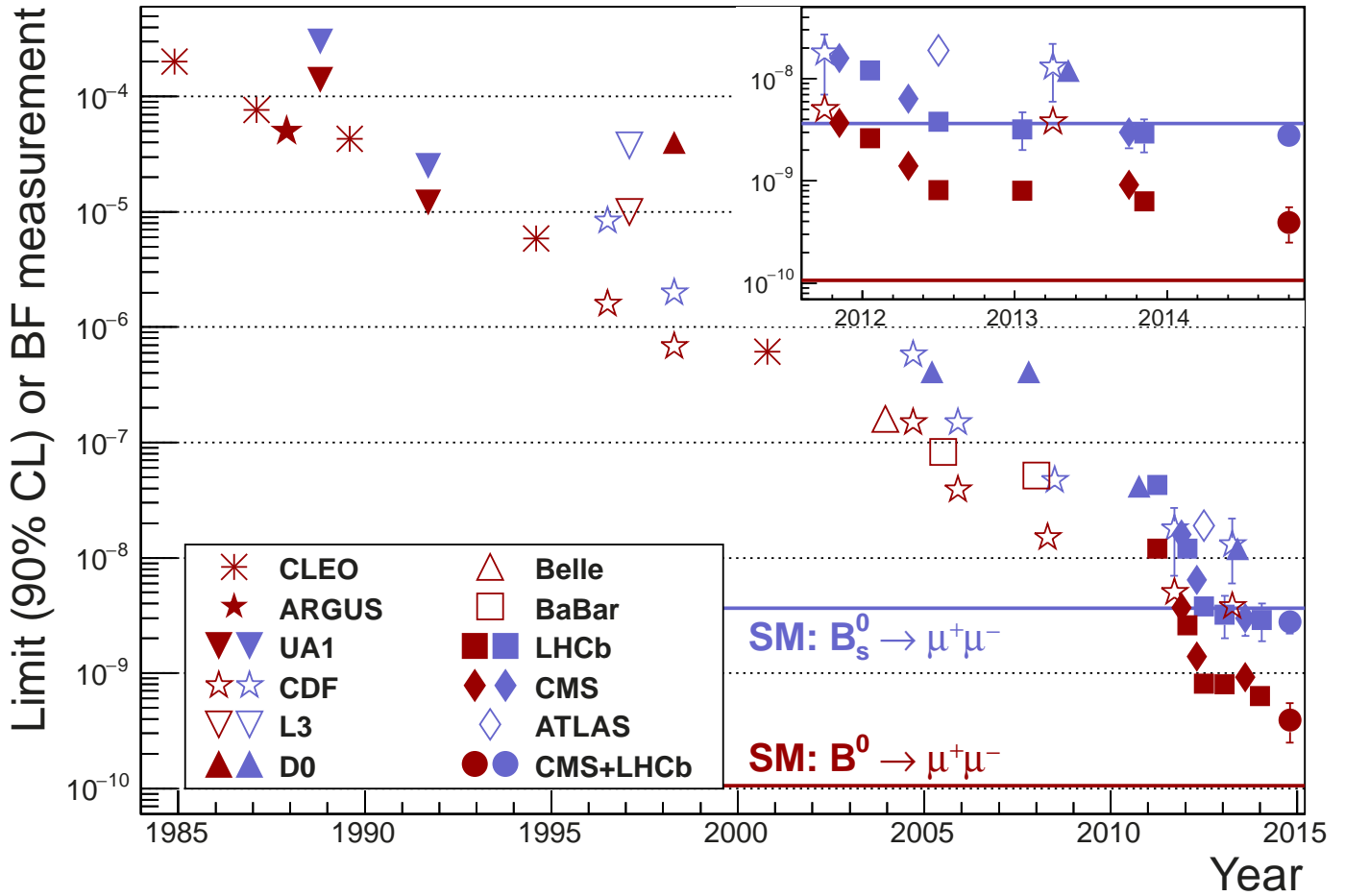
Extended Data Figure 5 | Confidence level as a function of the $\mathcal{B}(B^0 \rightarrow \mu^+ \mu^-)$ hypothesis. The value of $1 - \text{CL}$, where CL is the confidence level obtained with the Feldman–Cousins procedure, as a function of $\mathcal{B}(B^0 \rightarrow \mu^+ \mu^-)$ is shown in logarithmic scale. The points mark the computed $1 - \text{CL}$ values and the curve is their spline interpolation. The dark and light (cyan) areas define the two-sided $\pm 1\sigma$ and $\pm 2\sigma$ confidence intervals for the branching fraction, while

the dashed horizontal line defines the confidence level for the 3σ one-sided interval. The dashed (grey) curve shows the $1 - \text{CL}$ values computed from the one-dimensional $-2\Delta\ln L$ test statistic using Wilks' theorem. Deviations between these confidence level values and those from the Feldman–Cousins procedure³⁰ illustrate the degree of approximation implied by the asymptotic assumptions inherent to Wilks' theorem²⁹.



Extended Data Figure 6 | Likelihood contours for the ratios of the branching fractions with respect to their SM prediction, in the $S_{SM}^{B^0}$ versus $S_{SM}^{B_s^0}$ plane. **a**, The (black) cross marks the central value returned by the fit. The SM point is shown as the (red) square located, by construction, at $S_{SM}^{B^0} = S_{SM}^{B_s^0} = 1$. Each contour encloses a region approximately corresponding to the reported confidence level. The SM branching fractions are assumed

uncorrelated to each other, and their uncertainties are accounted for in the likelihood contours. **b**, **c**, Variations of the test statistic $-2\Delta\ln L$ for $S_{SM}^{B_s^0}$ and $S_{SM}^{B^0}$ are shown in **b** and **c**, respectively. The SM is represented by the (red) vertical lines. The dark and light (cyan) areas define the $\pm 1\sigma$ and $\pm 2\sigma$ confidence intervals, respectively.



Extended Data Figure 7 | Search for the $B_s^0 \rightarrow \mu^+ \mu^-$ and $B^0 \rightarrow \mu^+ \mu^-$ decays, reported by 11 experiments spanning more than three decades, and by the present results. Markers without error bars denote upper limits on the branching fractions at 90% confidence level, while measurements are denoted with error bars delimiting 68% confidence intervals. The solid horizontal lines

represent the SM predictions for the $B_s^0 \rightarrow \mu^+ \mu^-$ and $B^0 \rightarrow \mu^+ \mu^-$ branching fractions¹; the blue (red) lines and markers relate to the $B_s^0 \rightarrow \mu^+ \mu^-$ ($B^0 \rightarrow \mu^+ \mu^-$) decay. Data (see key) are from refs 17, 18, 31–60; for details see Methods. Inset, magnified view of the last period in time.